# On the production of ionospheric irregularities via Kelvin-Helmholtz instability associated with cusp flow channels

Andres Spicher<sup>1</sup>, Kshitija Deshpande<sup>2</sup>, Yaqi Jin<sup>1</sup>, Kjellmar Oksavik<sup>3,5</sup>,
Matthew D. Zettergren<sup>2</sup>, Lasse B. N. Clausen<sup>1</sup>, Jøran I. Moen<sup>1,5</sup>, Marc R.
Hairston<sup>4</sup>, and Lisa Baddeley<sup>5,3</sup>

Department of Physics, University of Oslo, Oslo, Norway

Department of Physical Sciences and Center for Space and Atmospheric Research (CSAR)

<sup>1</sup>Department of Physics, University of Oslo, Oslo, Norway

<sup>2</sup>Department of Physical Sciences and Center for Space and Atmospheric Research (CSAR),

Embry-Riddle Aeronautical University, Daytona Beach, FL, USA

<sup>3</sup>Birkeland Centre for Space Science, Department of Physics and Technology, University of Bergen,

Bergen, Norway

<sup>4</sup>Center for Space Sciences, University of Texas at Dallas, Richardson, TX, USA.

<sup>5</sup>University Centre in Svalbard, Longyearbyen, Norway

# **Key Points:**

10

11

12 13

16

- Observations and modelling work document that cusp flow shears can give rise to strong phase scintillations.
- The strongest phase scintillations occur in a region with inhomogeneous plasma flow and structured low-energy particle precipitation.
- Simulations show strong correlation between phase scintillations and turbulent structures from KHI, especially with high capacitance.

Corresponding author: Andres Spicher, andres.spicher@fys.uio.no

#### Abstract

21

22

23

25

26

27

28

29

30

31

32

33

34

35

37

38

39

40

41

42

43

44

45

48

49

50

51

52

53

55

56

57

60

61

62

63

64

65

68

69

70

We present a multi-instrument multi-scale study of a channel of enhanced, inhomogeneous flow in the cusp ionosphere occurring on 30 November 2014. We provide evidence that strong Global Navigation Satellite System (GNSS) phase scintillations indices ( $\sigma_{\phi}$  > 0.5 rad) can arise from such events, indicating that they are important in the context of space weather impacts on technology. We compare in detail two-dimensional maps of ionospheric density, velocity, and temperatures obtained by the European Incoherent Scatter Scientific Association Svalbard Radar with scintillation indices detected from a network of four GNSS receivers around Svalbard and examine the different sources of free energy for irregularity creation. We observe that the strongest phase scintillations occur on the poleward side of the flow channel in a region of sheared plasma motion and structured low-energy particle precipitation. As inhomogeneous plasma flows are evident in our observations, we perform a quantitative, nonlinear analysis of the Kelvin-Helmholtz instability (KHI) and its impact on phase scintillations using numerical simulations from the first principles based Geospace Environment Model of Ion-Neutral Interactions (GEM-INI) and Satellite-beacon Ionospheric-scintillation Global Model of the upper Atmosphere (SIGMA). Using representative values consistent with the radar data, we show that KHI can efficiently create density structures along with considerable scintillations, and is thus likely to contribute significantly under similar conditions, which are frequent in the cusp.

# 1 Introduction

The ionospheric cusps are complex systems where highly dynamic phenomena occur due to their coupling to the solar wind, the magnetosphere and the thermosphere. These phenomena include electron and ion precipitation, electrostatic and electromagnetic waves, as well as turbulence (e.g. Kelley & Carlson, 1977; Keskinen & Ossakow, 1983; Heppner et al., 1993; Cargill et al., 2005; Chaston et al., 2007; Carlson, 2012; Spicher et al., 2015, and references herein). At F region altitudes, this results in ionospheric density irregularities and turbulence, which are important for applications related to adverse effects of space weather on technology, as they can affect high frequency (HF) communication and cause amplitude and phase scintillations of transionospheric radio signals such as the ones used by Global Navigation Satellite Systems (GNSS) (e.g. Hey et al., 1946; Phelps & Sagalyn, 1976; Yeh, K. C. & Liu, C.-H., 1982; Kintner & Seyler, 1985; Tsunoda, 1988; Wernik et al., 2003; Kintner et al., 2007; Prikryl et al., 2011; Carlson, 2012; Moen et al., 2013; Spicher et al., 2015; Jin et al., 2019). With increased human activity in the Arctic, making progress at identifying and understanding the physical mechanisms that create these ionospheric irregularities, which can range from a few decameters to a few tens of kilometers, is of growing importance.

At high latitudes, several possible sources of free energy and instability mechanisms exist, and three categories have gained significant attention (e.g. Keskinen & Ossakow, 1983; Kintner & Seyler, 1985; Tsunoda, 1988; Wernik et al., 2003; Oksavik et al., 2011; Carlson, 2012; Moen et al., 2013): a) convective instabilities associated with density gradients (e.g. Keskinen & Ossakow, 1983; Tsunoda, 1988), b) particle precipitation driven irregularities (e.g. Dyson & Winningham, 1974; Keskinen & Ossakow, 1983) and c) flow shear related instabilities (e.g. Kintner & Seyler, 1985; Heppner et al., 1993; Ganguli et al., 1994; Keskinen et al., 1988). In particular, the gradient drift instability (GDI) operating on polar cap patches is often regarded as a dominant process for the creation of density irregularities (e.g. Simon, 1963; Linson & Workman, 1970; Weber et al., 1984; Basu et al., 1994, 1988; Gondarenko & Guzdar, 2004; Tsunoda, 1988; Oksavik et al., 2012; Lamarche & Makarevich, 2017; Makarevich, 2014, 2017; Forsythe & Makarevich, 2018).

Particle precipitation is also believed to play an important role for plasma structuring in the cusp region (Dyson & Winningham, 1974; Kelley et al., 1982; Keskinen & Ossakow, 1983, and reference therein). Indeed, low-energy ( $\leq 1000 \text{ eV}$ ) precipitating elec-

73

76

77

78

81

82

83

85

89

90

92

93

97

98

100

101

102

103

104

105

106

108

109

110

111

112

113

116

117

118

120

121

122

123

trons deposit most of their energy at F-region altitudes, and might be a source of density perturbations for large to medium scale irregularities ( $\lambda \geq 10$  km) (Rees, 1963; Dyson & Winningham, 1974; Kelley et al., 1982; Labelle et al., 1989; Millward et al., 1999). Moen et al. (2012) and Oksavik et al. (2012) suggested that the GDI could then further structure plasma gradients that were initially created by precipitation. Furthermore, Moen et al. (2002) hypothesized that the initial source of the decameter-scale perturbations associated with HF backscatter in the cusp might be the fine structures within particle precipitation itself.

Another source of energy can be found in flow shears, which are commonly found in the high latitude ionosphere in connection with discrete auroral forms (e.g. Oksavik et al., 2004a, 2005; Rinne et al., 2007; Moen et al., 2008). A relation between sheared plasma flow (inhomogeneous electric field) and broadband electrostatic turbulence and irregularities has been observed using rockets, satellites and from the ground (e.g. Kelley & Carlson, 1977; Basu et al., 1986, 1988; Earle et al., 1989; Heppner et al., 1993; Oksavik et al., 2004b, 2011, 2012; Spicher et al., 2016). Shears in the cross-field ion velocity can initiate the Kelvin-Helmholtz instability (KHI) (Keskinen et al., 1988), a mechanism regarded as important for the creation of irregularities in the cusp (Basu et al., 1988, 1994; Oksavik et al., 2011), and on which for instance the GDI (Carlson et al., 2007) or microscale instabilities (Ganguli et al., 1994) could develop, and further structure the plasma. One specific cusp phenomenon where cross-field sheared plasma flows and particle precipitation are fundamental is the Reversed Flow Event (RFE) (Rinne et al., 2007; Moen et al., 2008). RFEs are latitudinally narrow ( $\sim 50$  km to  $\sim 250$  km) and longitudinally extended (> 400-600 km) flow channels with flow direction opposite to that of the large-scale background convection (Rinne et al., 2007). They are common cusp features typically observed around magnetic noon and have a preference for interplanetary magnetic field (IMF)  $|B_y| > |B_z|$  (Rinne et al., 2007; Moen et al., 2008; Oksavik et al., 2011). RFEs are believed to be signatures of a flux transfer event (FTE) (Southwood, 1987), and are related to the brightening of Birkeland current arcs (Oksavik et al., 2004a, 2005; Moen et al., 2008). Decameter-scale density irregularities have been observed in relation to RFEs, and it was proposed that the KHI and micro-scales instabilities could be responsible for their creation (e.g. Oksavik et al., 2011; Carlson et al., 2007; Spicher et al., 2016). RFEs are therefore cusp phenomena that are particularly interesting in the framework of space weather and flow shear instabilities (Moen et al., 2013).

Space weather studies based on ground-based GNSS data at high latitudes are numerous and include (not inclusive) statistical surveys (e.g. Spogli et al., 2009; Alfonsi et al., 2011; Prikryl et al., 2011, 2015; Jin et al., 2018b) and studies targeting specific ionospheric phenomena such as polar cap patches (e.g. Mitchell et al., 2005; Jin et al., 2014, 2016; van der Meeren et al., 2015; Zhang et al., 2017), the storm enhanced density (SED)/tongue of ionization (TOI) (e.g. van der Meeren et al., 2014; Wang et al., 2016, 2018), auroral blobs (Jin et al., 2014, 2016), periods of extended dayside reconnection (Clausen et al., 2016), cusp aurora (poleward auroral moving forms) (Jin et al., 2015; Oksavik et al., 2015), auroral arcs (e.g. van der Meeren et al., 2016; Forte et al., 2017; Semeter et al., 2017), cusp dynamics with or without polar cap patch production (Jin et al., 2017). However, despite the significant amount of studies, the physical causes for the development of the small-scale irregularities and associated enhanced scintillation observed are still not clear. In particular, the applicability and importance of different instability modes (e.g., KHI) in the high-latitude ionosphere remains to be tested.

Here, we present a multi-instrument multi-scale study of a cusp flow channel (including an RFE) identified using the European Incoherent Scatter Scientific Association (EISCAT) Svalbard Radar (ESR) and leading to enhanced phase scintillations. Then, as velocity shears are evident in our data and due to the prevalence of inhomogeneous flows near the cusp (e.g. Heppner et al., 1993; Clauer, 2003; Oksavik et al., 2004b, 2005; Carlson et al., 2008; Rinne et al., 2007; Moen et al., 2008) where phase scintillations peak

(Prikryl et al., 2015; Jin et al., 2015, 2017), we place our observations in the context of the KHI process. We do not intend to rule out GDI or precipitation (or alternative possibilities) as playing a role in the scintillation for the specific event however, our main motivation is to test KHI and its impact on scintillations. Thus, we perform a quantitative, nonlinear analysis of KHI using numerical simulations from the Geospace Environment Model of Ion-Neutral Interactions (GEMINI) and Satellite-beacon Ionospheric-scintillation Global Model of the upper Atmosphere (SIGMA) and examine and discuss its potential role in creating cusp ionospheric irregularities and scintillations.

# 2 Instrumentation and numerical models

In this study, the large-scale context is obtained from the Super Dual Auroral Radar Network (SuperDARN) (Chisham et al., 2007) and GPS Madrigal total electron content (TEC) maps (Rideout & Coster, 2006; Vierinen et al., 2016), while data from ESR (Wannberg et al., 1997) and from the Defense Meteorological Satellite Program (DMSP) F17 (Hairston, 2019; Redmon et al., 2017) provide details about the mesoscale structures. Irregularities smaller than a few kilometers are considered using GNSS data obtained from a network of four receivers around Svalbard (Oksavik et al., 2015) and SuperDARN spectral width observations (Kintner et al., 2007; Chisham et al., 2007). Furthermore, numerical simulations are performed to supplement the observations. The different instruments and models used are briefly presented in this section.

For completeness, we first briefly describe the solar wind conditions around the time of the event, i.e., around 09:37 UT to 10:00 UT on 30 November 2014. This includes the Interplanetary Magnetic Field (IMF) in geocentric solar magnetospheric coordinates (GSM), the solar wind velocity, and the proton density from the 1-min resolution OMNI data set (King & Papitashvili, 2005). The quantities have already been shifted to the observation site from the nose of the Earth's bow shock (King & Papitashvili, 2005).

We use SuperDARN data to map the large-scale context surrounding the mesoscale flow channels detected by the ESR. We present velocity vectors derived by merging data from the Hankasalmi and Pykkvibær radars. The line-of-sight velocity data from both radars are mapped onto an equal-area grid in the vicinity of the ESR field-of-view and aggregated over six minutes, as a compromise between data coverage and temporal resolution. Line-of-sight flow measurements within one grid cell are merged to form a two-dimensional (2D) flow vector, whenever both radars contribute (e.g. Ruohoniemi et al., 1989). The spectral width is computed in a similar manner.

We use data from four NovAtel GPStation-6 GNSS Ionospheric Scintillation and TEC Monitors installed in the Svalbard archipelago. The receivers are located in Ny-Ålesund (NYA; 78.9°N, 11.9°E), at the Kjell-Henriksen Observatory in Longyearbyen (LYB; 78.1°N, 16.0°E), in Hopen (HOP; 76.5°N, 25.0°E), and on Bear Island (BJN; 74.5°N, 19.0°E) (van der Meeren et al., 2015). The receivers are operated by the University of Bergen and track signals at several frequencies from GPS, GLONASS, and Galileo (Oksavik et al., 2015). The receivers output the phase scintillation index  $\sigma_{\phi}$  (Fremouw et al., 1978; Rino, 1979), which is computed over 60 s from the raw carrier phase and detrended using a sixth-order Butterworth high-pass filter with the conventional frequency of 0.1 Hz (Van Dierendonck et al., 1993). The 60 s amplitude scintillation index  $S_4$  (Briggs & Parkin, 1963), the total TEC, and the rate of TEC (ROT) are also provided (Oksavik et al., 2015).

It is worth noting that  $\sigma_{\phi}$  is not without issues. The index is sensitive to the cutoff frequency (0.1 Hz), which may include refractive contributions from larger scale irregularities at high latitudes (e.g. Forte & Radicella, 2002; Beach, 2006; Mushini et al.,
2012; Wang et al., 2018; McCaffrey & Jayachandran, 2019). This issue is however not

crucial for the purpose of our paper, i.e. to use  $\sigma_{\phi}$  as a proxy for the presence of den-

sity irregularities. Also, for completeness, spectrograms of the raw phase data are shown in the supporting material in Figure S3. Those may indeed provide further information about the scales of the irregularities involved and overcome issues related to the  $\sigma_{\phi}$  index as suggested by van der Meeren et al. (2014, 2015). Furthermore, geometric enhancements of scintillations may occur when the signal path is parallel to the irregularity axis. At the onset of enhanced phase scintillations, the elevation angle of the satellites of interest ranged between around 32° degrees to around 42°, roughly corresponding angles of about 40° to about 50° between the signal path and the magnetic field, which had local dip angles greater than 82° (calculated using International Geomagnetic Reference Field-12 (Thébault et al., 2015)). Thus, we do no expect this to be a critical issue for the purpose of this study.

We use the L1 frequency for scintillation, and dual frequencies for TEC (L1 and L2Y for GPS, L1 and L2P for GLONASS). No Galileo satellite was tracked during the time of interest. For TEC we calculate the vertical TEC (vTEC) (Mannucci et al., 1993; Alfonsi et al., 2011). The data have been scrutinized to filter out multi-path effects using long-term observations for each stations but we also apply a cutoff elevation angle of 25° for all receivers to minimize remaining errors. The GNSS ionospheric pierce points (IPPs) have been projected to 300 km altitude, which roughly corresponds to the peak electron density observed by the magnetic field-aligned fixed 42 m ESR dish (shown in Figure S3 in the supporting information).

We use the fully steerable ESR 32 m antenna (Wannberg et al., 1997) for deriving 2D maps of densities, velocities and temperatures. The scans were performed in azimuth at a fixed elevation angle of  $30^{\circ}$ , providing "fan plots" of the ionospheric plasma conditions with an integration time of 6.4 s (Carlson et al., 2002). In the rest of the paper, the abbreviation ESR always refers to the 32 m dish.

In addition, we use in situ measurements right above the ESR field of view. These were obtained by DMSP F17, which has an orbital period of about 101 min at around 840 km altitude (e.g. Rich & Hairston, 1994; Kilcommons et al., 2017). We use the level 2 data obtained at a cadence of 1 sec from the Special Sensors-Ions, Electrons, and Scintillation (SSIES) instruments, and show ion and velocity data from the Retarding Potential Analyzer (RPA) and from the Ion Drift Meter (IDM), respectively (Rich, 1994b; Hairston, 2019). Data with quality flags "poor" are removed. We also use the new DMSP database of precipitating electrons and ions obtained from the Special Sensor J (SSJ) 5 instrument (Redmon et al., 2017), which measures fluxes from 30 eV to 30 keV each second (Hardy et al., 2008).

Numerical models are also used in this study. The GEMINI model (Geospace Environment Model of Ion-Neutral Interactions) is a 3-dimensional (3D) multifluid-electrodynamic model of high latitude ionospheric plasma instabilities (Zettergren et al., 2015). GEM-INI includes both aeronomical, transport, and electrodynamic processes relevant to the formation of ionospheric fluid instabilities such as GDI and KHI (e.g. K. B. Deshpande & Zettergren, 2019). The model comprises a fluid system of equations (Schunk, 1977; Blelly & Schunk, 1993), describing dynamics of the ionospheric plasma, self-consistently coupled to an quasi-electrodynamic treatment of auroral and neutral dynamo currents (Zettergren et al., 2015). The fluid system is a set of three conservation equations (mass, momentum, and energy) for each ionospheric species s relevant to the E-, F-, and topside regions  $(s = O^+, NO^+, N_2^+, O_2^+, N^+, H^+)$ . Terms in the conservation of mass equations encapsulate chemical production and impact ionization (via the method of (Fang et al., 2008) or the GLOW energetic electron transport code of (Solomon & Qian, 2005)) and chemical loss (taken from Diloy et al. (1996); St-Maurice and Laneville (1998), and references therein), while photoionization sources are calculated according the method presented in Solomon and Qian (2005) using solar fluxes from the EUVAC model (Richards et al., 1994). GEMINI's momentum equations includes time-dependence and ion inertial effects relevant to plasma instabilities of interest, as well as pressure, gravity, electromagnetic and collisional drag forces. Full ion and electron energy equations are also solved by GEMINI.

SIGMA (Satellite-beacon Ionospheric-scintillation Global Model of the upper Atmosphere) is a three-dimensional (3D) electromagnetic wave propagation model capable of simulating scattering, diffraction, wave refraction and reflection through an arbitrary density field - including a turbulent plasma simulated by a physics-based model like GEMINI. SIGMA handles propagation of a radio frequency signal from a moving satellite to the ground through multiple phase screens (MPS) anywhere on the globe (Deshpande et al., 2014). The model is especially applicable at high latitudes where the magnetic field inclination is changing with the location, making the geometry complicated. Inside SIGMA, first a spatial electron number density distribution from a spectral model for irregularities or the number density itself from a plasma model (such as GEMINI) translated into phase screens is inserted, and then the signal is propagated between the multiple phase screens and to the ground. SIGMA outputs 2D complex signal propagated to the ground as well as high rate GPS scintillation phase and power time series with 50 Hz sampling frequency, from which S4 and  $\sigma_{\phi}$  can be easily extracted. High rate phase and power are detrended and filtered in order to eliminate any low frequency effects including the satellite motion (Van Dierendonck et al., 1993).

For this paper, we simulate the time-dependent evolution (through both linear and nonlinear stages) of KHI with GEMINI and then use SIGMA to propagate GPS signal from satellite vehicle number PRN G28 through simulated KHI electron density irregularities at the time of interest (on 30 November 2014); the methodology is an extension of that applied to study GDI in prior related work (K. B. Deshpande & Zettergren, 2019).

# 3 Data presentation

229

230

231

232

233

234

237

238

239

240

241

242

245

246

249

250

251

252

253

255

256

257

258

262

263

265

266

268

269

270

271

272

274

275

276

In this section, we present the observations from the different instruments described in section 2. We first outline the large-scale context and then zoom into the meso- and smaller-scale observations.

## 3.1 Large-scale context

The solar wind conditions were relatively stable around the time of the event, i.e., between about 09:37 UT and 10:00 UT on 30 November 2014. For completeness, a figure showing OMNI data is given in the additional material in Figure S1 and the main characteristics of the solar wind during the interval of interest are described below. The IMF  $B_x$  component was positive with values ranging between about 9 nT and 4 nT, while the IMF  $B_y$  component decreased from 0 nT to about -9 nT right after 09:40 UT. IMF  $B_y$  then remained quite stable around -9 nT. The IMF  $B_z$  component turned slightly negative at about 09:38 UT (with values close to -3 nT), remained negative for about 15 minutes, and increased to close to zero from about 09:52 UT. The solar wind velocity took values between about 375 km/s and 395 km/s between about 09:37 UT and 10:00 UT, and the proton density ranged between 6 and 9 particles per cubic meter.

In order to frame the large-scale ionospheric flow context above Svalbard during the time of the event, we use the Doppler drift velocity data from SuperDARN radars, shown in Figure 1. The coordinates are Altitude Adjusted Corrected Geomagnetic Coordinates (AACGM) (Baker & Wing, 1989), with magnetic local time (MLT) shown on the bottom of each panel. Geomagnetic North  $(N_m)$  is roughly on the top of each panel, as illustrated by the blue arrow. The solid black line shows the ESR field of view and the red box highlights the region with largest phase scintillation indices (presented in detail below). The black arrows illustrate the velocity vectors derived by combining data from the Hankasalmi and Pykkvibær radars, and the grey arrows show line-of-sight ve-

locities from single radars, i.e. when it was not possible to combine the data from the two radars.

283 286 287

During the time of the event, Syalbard was located postnoon at around 13 MLT, with the ESR field of view being located around 12 MLT. Between 09:36 UT and 09:42 UT, the large scale plasma flow above and north of Svalbard was directed towards southwest, as seen in Figure 1 a). This flow motion reversed completely between 09:42 UT and 09:48 UT, as shown in 1 b): the large scale plasma motion was now generally poleward. Between 09:48 UT and 09:54 UT the poleward (northeast) flow displayed in 1 c) intensified significantly and, in the field of view of ESR, it reached values of about 1000 m/s

north of Svalbard. During the next 6 minutes enhanced poleward plasma circulation remains visible in Figure 1 d) (this goes on until about 10:10 UT, not shown).

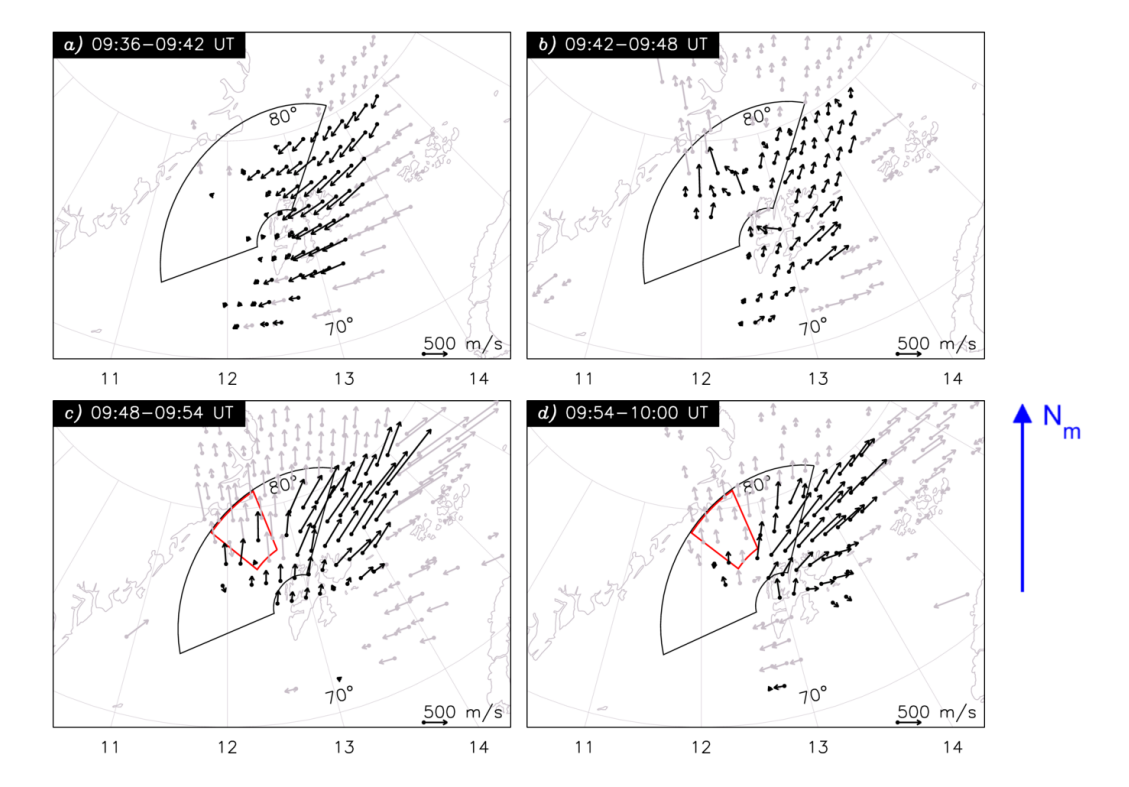


Figure 1. SuperDARN velocity vectors (black arrows) derived by combining data from the Hankasalmi and Pykkvibær radars and integrated over 6 minutes. The grey vectors show lineof-sight velocities from single radars where not enough data from both radars was available to produce 2D flow vectors. Coordinates are AACGM with MLTs shown on the bottom of each panel. North is roughly on the top of each panel, as illustrated by the blue arrow. The fan shape shows the ESR field of view and the red box highlights the region with largest phase scintillation indices.

288 292 293

To frame the large-scale background density, Figures 2 a1) to a4) display four GPS TEC maps around Svalbard using data from the Madrigal database (Rideout & Coster, 2006; Vierinen et al., 2016). Geographic north is on the top of the each panel and the blue arrow with label  $N_m$  shows the direction to geomagnetic North. For better visualization, each TEC map has been averaged using a median filtering process including the previous and the next GPS TEC maps (Thomas et al., 2013). In addition, each panel shows five minutes of phase scintillation indices  $\sigma_{\phi}$  centered around the times shown in

the top right corners. The phase scintillation index is displayed as dots for low phase scintillation ( $\sigma_{\phi} < 0.25$  rad), medium circles for intermediate phase scintillation ( $0.25 \le \sigma_{\phi} < 0.5$  rad), and big circles for strong phase scintillation ( $\sigma_{\phi} \ge 0.5$  rad). A few selected PRNs detected from the NYA receiver are highlighted using different colors, with the letter "R" standing for GLONASS and "G" for GPS. The fan-shaped line shows the ESR field of view.

As can be seen in Figure 2 a1), the event began with the presence of a region of enhanced density poleward of Svalbard, hereafter referred to as "the density reservoir". This region is highlighted by the dotted oval. The enhanced solar EUV plasma density can be seen further south separated by a region with low density above Svalbard, i.e. a trough. Comparing with SuperDARN data shown in Figure 1 a), this corresponds to the time interval during which the flow reversed from approximately sunward to antisunward. In general, the phase scintillation level observed was low in the entire field of view. In Figure 2 a2), the TEC map remains quite similar with a slight poleward motion of the high density reservoir. In this panel, enhanced phase scintillation indices appear between the large density at high latitudes and the trough. Values of  $\sigma_{\phi} \geq 0.5$  rad persisted in the same region in panel a3) and a4), during which a clear poleward motion of the high density region can observed. This is consistent with the large-scale flow pattern observed by SuperDARN in Figure 1 c) and d). In the end, the electron density was low in the field of view of ESR, but  $\sigma_{\phi}$  remains enhanced.

To better visualize the evolution of the GNSS measurements, Figure 2 b) to m) shows the time series for selected PRNs detected from NYA. G11 was chosen to illustrate observations at lower latitudes in the trough while R12, R22 and G28 were initially close to the boundary between the trough and the density reservoir and detected the strongest phase scintillation indices. R13 is also shown as it detected enhanced phase scintillation indices at higher latitudes. Panels b), c) and d) show vTEC with respect to time. In panel b), vTEC takes values below about 10 TECU, consistent with the density trough observed in the TEC maps. In panel c) and d), vTEC is relatively constant until about 09:48-09:49 UT, after which it decreases. At the end of the interval, the vTEC values observed from NYA in the northern portion of the ESR are similar to vTEC in the trough, consistent with panel a4). In panels b), c) and d), vTEC also becomes relatively more irregular with time. This can be better seen by looking at the absolute value of the ROT shown in panels e), f), and g): |ROT| is larger from the middle of the interval. A maximum of 4 TECU/min is reached at 09:50 UT for R22 and R12 in panel f) and at 09:51 UT for R13 in panel g).

Figure 2 h), i), and j) shows the amplitude scintillation index  $S_4$  with respect to time. The values remain low with some small increases in panel j) and k).

Panels k), l) and m) display the phase scintillation index  $\sigma_{\phi}$  with respect to time. In the density trough,  $\sigma_{\phi} < 0.2$  rad during the entire time interval, as can be seen in panel l). The onset of large phase scintillation index is detected by PRNs R12, R22 and G28 at 09:49 UT while PRN R13 sees a maximum in  $\sigma_{\phi}$  about 3 minutes later. The enhanced values of  $\sigma_{\phi}$  are not observed in the regions with largest vTEC, but coincide with the decrease in vTEC observed in panel c) and d).

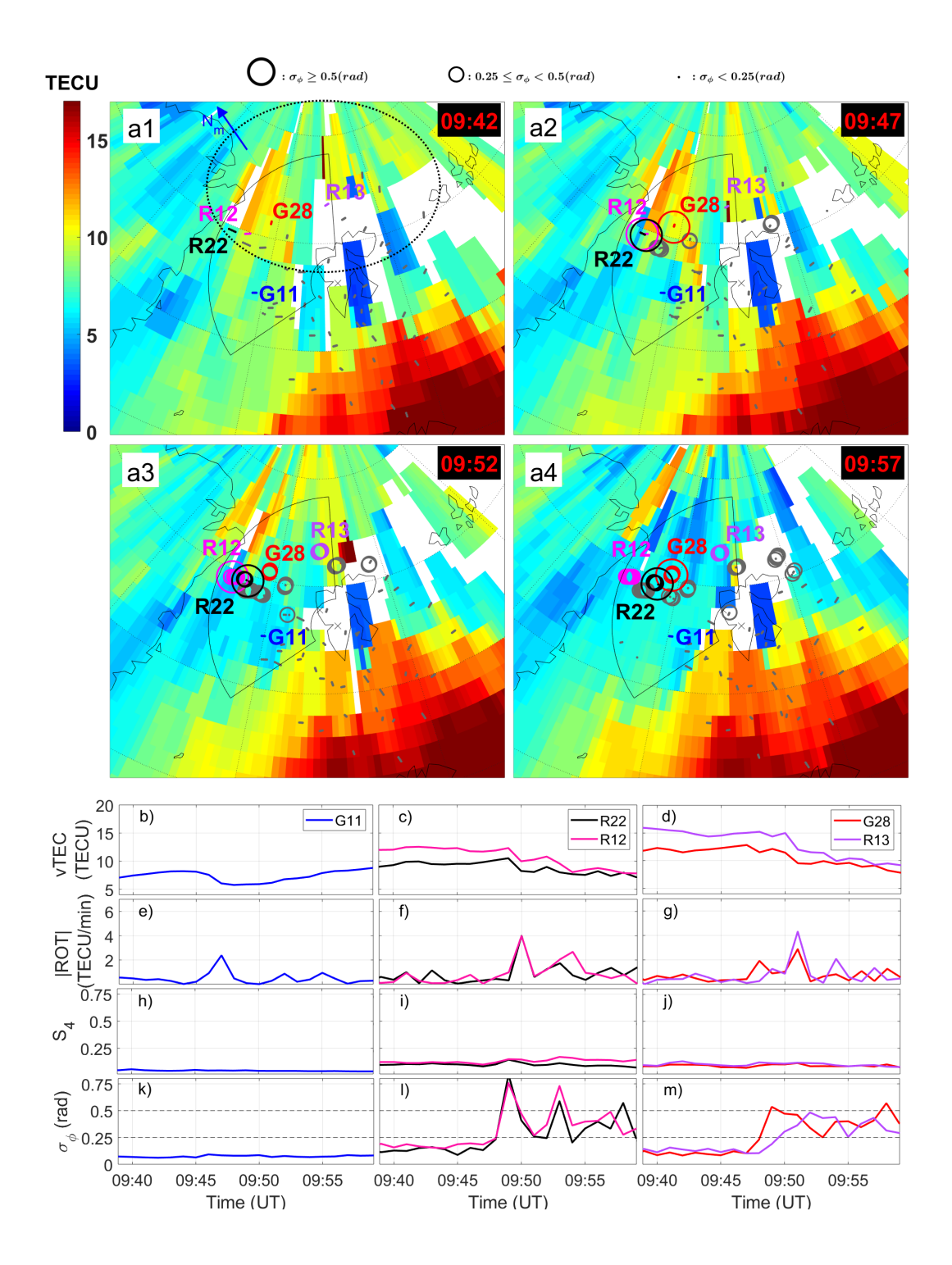


Figure 2. a1 to a4) GPS TEC maps for four time intervals of 5 minutes using data from the Madrigal database with phase scintillation indices obtained from four receivers on Svalbard overlaid. The phase scintillation level is displayed as black dots for low scintillations ( $\sigma_{\phi} < 0.25$  rad), medium circles for intermediate scintillations ( $0.25 \leq \sigma_{\phi} < 0.5$  rad), and big circles for strong scintillations ( $\sigma_{\phi} \geq 0.5$ ). The colored numbers highlight selected PRNs tracked from the receiver at Ny-Ålesund. The letter "R" stands for GLONASS and "G" for GPS. The fan-shaped solid line shows the ESR field of view while the dotted oval in a1) highlights the density reservoir. Panels b) to m) show the time series of vTEC (b,c,d), |ROT| (e,f,g),  $S_4$  (h,i,j), and the phase scintillation index  $\sigma_{\phi}$  (k,l,m) for the selected PRNs between 09:37 UT and 10:00 UT.

#### 3.2 Meso- and small-scale observations

338

339

340

341

342

343

344

347

348

349

350

351

352

354

355

356

Now that the large-scale framework has been presented, insights into the meso-scale configuration can be obtained from ESR. Figure 3 shows four ESR fan plots labelled with  $S_0$  to  $S_3$  in geographic coordinates. For visualization purpose and comparison with SuperDARN, a blue arrow points towards geomagnetic north  $(N_m)$  and the same red box as in Figure 1 is shown in the last panel. Each row corresponds to one scan covering  $120^{\circ}$ in azimuth in 192 s. The GNSS data from all four receivers are superimposed on the ESR scans. The GNSS vTEC is color-coded while the phase scintillation level is displayed as black dots for low phase scintillation ( $\sigma_{\phi} < 0.25 \text{ rad}$ ), medium circles for intermediate phase scintillation (0.25  $\leq \sigma_{\phi} <$  0.5 rad), and big circles for strong phase scintillation  $(\sigma_{\phi} \geq 0.5 \text{ rad})$ . The first column shows the electron density  $(N_e)$  measured by ESR with vTEC. The second column shows ESR ligne-of-sight ion velocity  $v_i$  and  $\sigma_{\phi}$ . The third and fourth columns show  $\sigma_{\phi}$  with the ESR electron temperature  $(T_e)$  and the ESR ion temperature  $(T_i)$ , respectively. The altitudes (200 km, 300 km and 400 km) of the ESR beams are also displayed as black lines. Note that the data above 400 km in regions with low density is quite uncertain (with errors that can be larger than 50% in some bins). It is however kept here to show the full ESR scan beams. For visualization purpose, the PRNs are not repeated, but the red arrow points toward PRNs R22, R12 and G28, while the black arrow towards  $G_{11}$ . The time history of the event shown in Figure 3 is presented in detail in the following.

Figure 3. Each row (labelled with  $S_0$  to  $S_3$ ) is an ESR fan plot with the corresponding scanning time shown in black in the center. "cw" and "ccw" stand for clockwise scan and counterclockwise scan, respectively. Left column: ESR density and GNSS vTEC. Second column: ESR ion line-of-sight velocity  $v_i$ . Third column: ESR electron temperature  $T_e$ . Fourth column: ESR ion temperature  $T_i$ . The black dots and circles illustrate different phase scintillation levels. The magenta line and times (in UT) in the bottom row illustrate the orbit of DMSP F17. The red and black arrows highlight regions of interest and the red box is the same as the one in Figure 1.

In the first scan shown here,  $\mathbf{S_0}$  (from 09:37:37 UT to 09:40:49 UT), a reservoir of high density can be observed poleward of Svalbard above 200 km altitude (red and orange region in ESR Ne and vTEC in the top left panel, highlighted by the red arrow),

equatorward of which a trough of low density can be observed (blue region in ESR Ne and vTEC, highlighted by the black arrow). At F-region altitudes, densities take representative values of  $4 \cdot 10^{11}~m^{-3}$  and  $1.5 \cdot 10^{11}~m^{-3}$  in the reservoir and trough, respectively. A broad region of westward flow with median velocities reaching about 700 m/s (yellow, away from the radar) can be seen above Svalbard, i.e., in the trough region, and directed towards the radar at higher latitudes (blue, towards the radar) with velocities of about -100~m/s. This is generally consistent with the SuperDARN velocities shown in Figure 1 a), exhibiting a southwest flow. No significant enhancements in the electron and ion temperatures can be observed. During that time interval, the phase scintillation level is low.

In the next scan,  $S_1$  (from 09:40:49 UT to 09:44:01 UT), the trough and higher density reservoir are still present, in agreement with the TEC map shown in Figure 2 a1). No significant enhancements in ESR  $T_e$  and  $T_i$  can be observed. In the velocity scan, the broad region of westward flow has turned into a narrower flow channel (yellow) with velocities reaching values of about 600-800 m/s. The flow outside of this channel is generally in the opposite direction (blue) with median velocities (between about 200 km and 350 km altitude) of about -150 to -200 m/s. The equatorward side of the flow channel is located in the density trough and the poleward side near the boundary between the trough and the higher density northward. The phase scintillation level is still low.

In the next scan,  $S_2$  (09:44:01 UT to 09:47:13 UT), the density trough and reservoir are still similar. The flow channel has moved slightly poleward and exhibits velocities reaching 900 m/s, while the plasma motion towards the radar (blue) on its flanks reach values of about -500 m/s. This implies maximum velocity differences  $\Delta V \approx 1400$ m/s. In addition, a (geographic) poleward flow of about 500 m/s north of Svalbard is now visible, in accordance with the large-scale convection pattern seen by SuperDARN in Figure 1 b) and the GPS TEC map in Figure 2 a2). A new feature in this scan is the appearance of a thin East-West channel of enhanced  $T_e$  between 300 km and 400 km, collocated with the polweard side of the flow channel. Low-energy cusp particle precipitation will result in enhanced  $T_e$  in the cusp ionosphere (Vontrat-Reberac et al., 2001), which is often seen in connection with auroral arcs (Weber et al., 1989; Valladares & Carlson Jr., 1991; Doe et al., 2001). The channel of enhanced  $T_e$  in Figure 1  $S_2$  is therefore interpreted as a signature of active cusp precipitation and auroral emissions. The conditions are sill relatively quiet, with a low scintillation level in general. In the ESR field of view, an increase of the phase scintillation index (to  $0.25 \le \sigma_{\phi} < 0.5$  rad) can however be observed at the poleward boundary of the flow channel, i.e. close to sheared-flow, and near the region of enhanced  $T_e$ . This is also located in the high density reservoir (close to the red arrow) near the boundary between the low and high density regions and in the shear region. On the other hand, there are still no significant increases in the phase scintillation indices on the equatorward side of the RFE in the trough (highlighted with the black arrow).

During the next scan,  $S_3$  (from 09:47:13 UT to 09:50:25 UT, i.e., after about 10 min to 13 min since  $S_0$ ), the trough and high density reservoir are still present. The flow channel has moved slightly poleward since  $S_2$  and is less uniform, but with similar velocity magnitudes (slightly larger). The reversed flow poleward of the flow channel matches the definition of an RFE (Rinne et al., 2007). The poleward motion north of Svalbard is also still present, consistent with SuperDARN Figure 1 c) and Figure 2 a2). The channel of enhanced  $T_e$  has now expanded equatorward into a broad region above 180-200 km altitude. This may indicate the presence of broader region of cusp particle precipitation. The poleward region of this enhancement in  $T_e$  matches the RFE region (blue  $v_i$ ), and the equatorward part extends to the middle of the trough. At this stage, enhancements in  $T_i$  to about 2500 K also appear above about 200 km altitude. During this scan, enhanced phase scintillation indices are detected in the RFE on the poleward side of the flow channel and of the region with enhanced  $T_e$ . This is also collocated with the area

exhibiting ion heating. On the other hand, no significant scintillations are observed in the density trough on the equatorward side of the flow channel (black arrow).

During scan  $S_3$ , DMSP F17 orbits above the field of view of ESR between about 09:49 UT and about 09:51 UT, as indicated by the magenta line. The observations made by DMSP F17 are shown in Figure 4 a), b), and c), with a magenta box highlighting the interval during which DMSP orbits above the region of interest. For visualization purposes scan  $S_3$  is also shown (only  $N_e$ ,  $v_i$  and  $T_e$ ) with the magenta part of the trajectory corresponding to the magenta box. Figure 4 a) depicts the ion density, which is quite irregular. One larger peak with steep gradients can be seen at about 09:49:30 UT, and one at 09:50:00 UT.

Panel b) shows two components of the ion velocity measured on-board DMSP F17; the horizontal cross-track component (dark blue,  $v_{\perp}$ ) with negative sign being approximately anti-sunward, and the upward component (cyan,  $v_z$ ). Both components are highly inhomogeneous with several intervals of fast flows ( $\geq 2000 \text{ m/s}$ ), and several gradients in the region of interest. In particular, a flow channel with a maximum of -2921 m/s reached at 09:50:36 UT can be observed. This is collocated with the location of the flow channel, as can be seen in the ESR  $v_i$  scan (yellow, away from the radar).

Figure 4 c) shows the electron precipitation differential energy flux (color coded), with the average energy  $(E_{av})$  displayed as a black line. From about 09:49:45 UT to about 09:52:00 UT, the average energy of precipitating electrons ranges between about 100 eV and 300eV. This roughly corresponds to the time interval during which DMSP orbits above the region of enhanced ESR  $T_e$ , supporting that it is due to low-energy "soft" particle precipitation (Weber et al., 1989; Valladares & Carlson Jr., 1991; Vontrat-Reberac et al., 2001; Doe et al., 2001). In this interval, electron precipitation is finely structured into short bursts with typical lengths of 1 to 2 seconds (corresponding to  $\sim 8-16$  km). This is especially pronounced between 09:49:45 UT and 09:51:00 UT. This interval matches the poleward region of enhanced  $T_e$  observed above 180-200 km altitude in the ESR scans. Noteworthy is also the coincidence between the two largest electron fluxes in the interval of interest and the density enhancements previously mentioned at 09:49:45 UT and 09:51:00 UT (compare with Figure 4 a)).

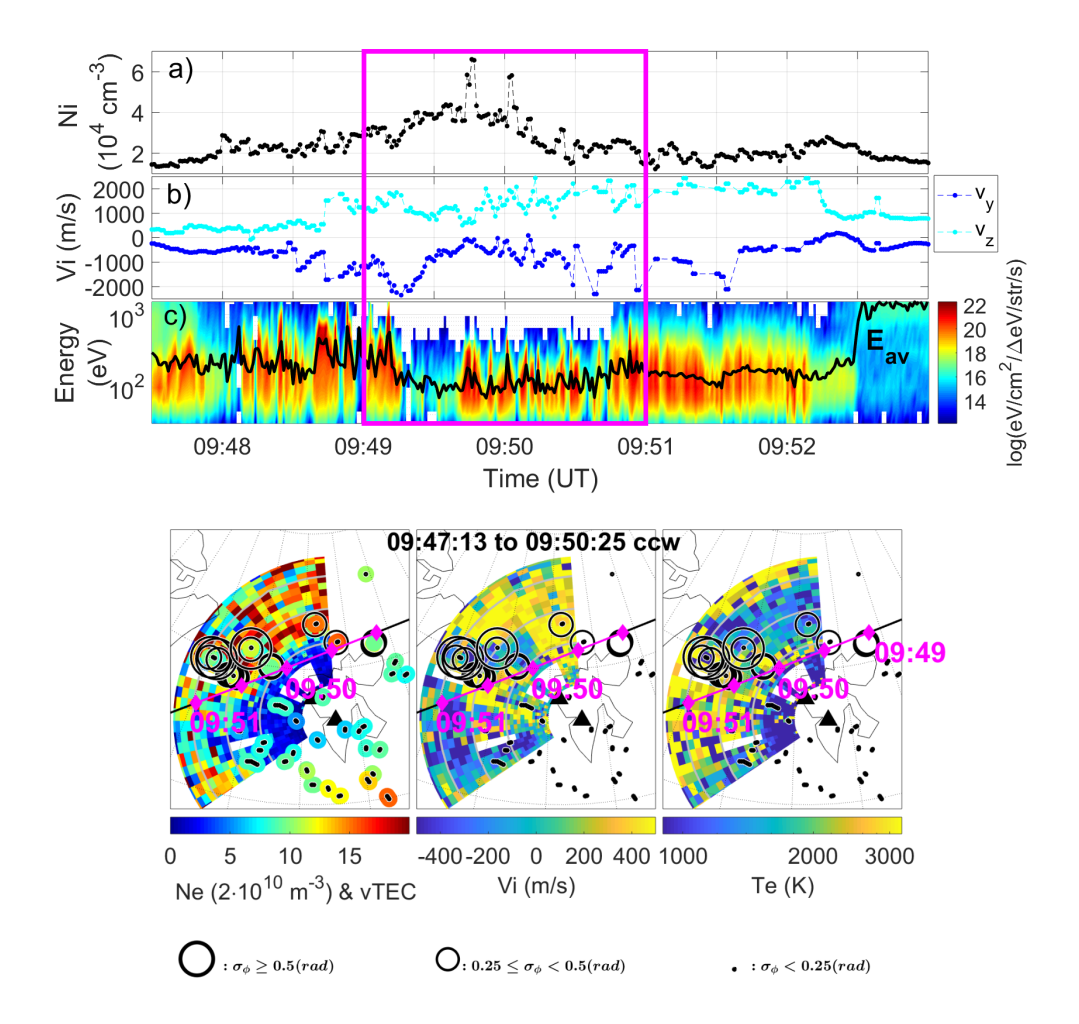
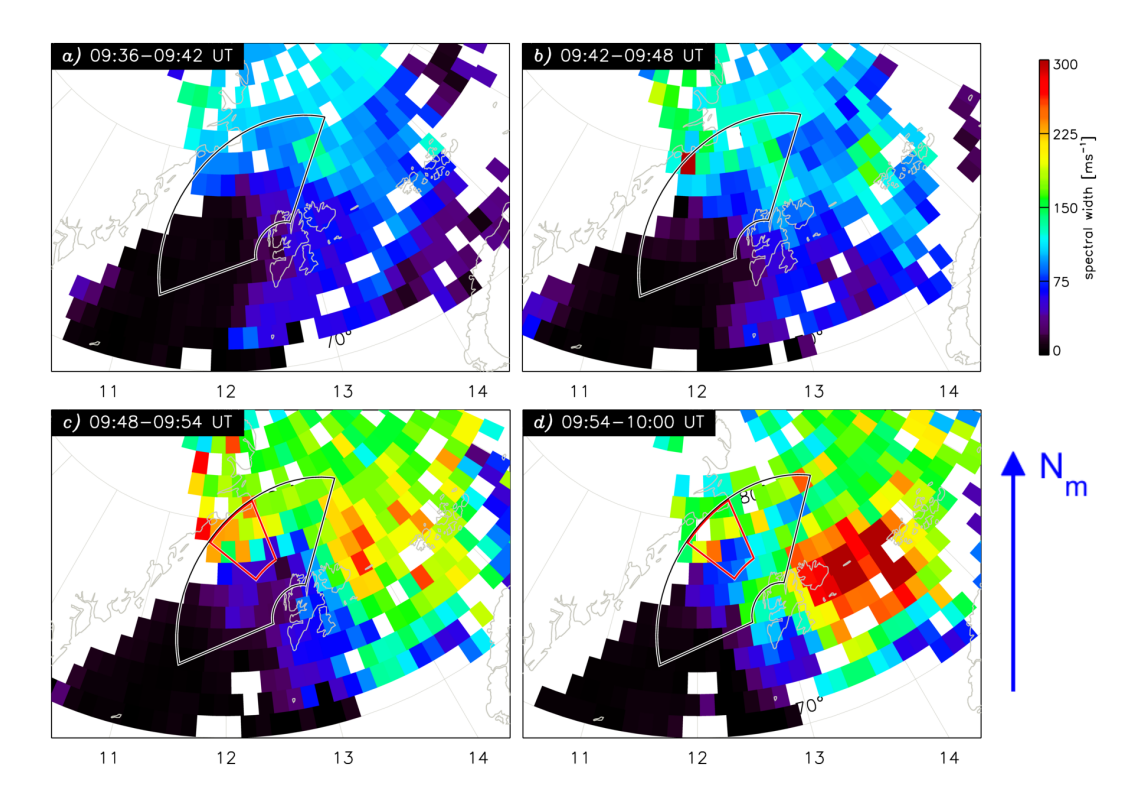


Figure 4. a) Ion density measured on-board DMSP F17. b) Horizontal cross-track velocity  $(v_y, \text{ dark blue})$ , and upward cross-track velocity  $(v_z, \text{ cyan})$  obtained from DMSP F17. c) Electron particle precipitation spectrum (color coded) and average energy  $E_{av}$  (black line) measured by DMSP F17. The magenta box illustrate the time interval during which DMSP F17 flew over the Svalbard region. In the bottom part of the figure, the ESR scan at the time of conjunction between the radar and DMSP is shown. This corresponds to scan  $S_3$  Figure 3. The magenta part of the orbit corresponds to the time range of the magenta box.

As presented in Figure 2, the conditions remained perturbed after the onset of enhanced phase scintillations around 09:49 UT. According to the three next ESR scans (shown in the supporting material in Figure S2), enhanced phase scintillation indices persist during the next ten minutes in the vicinity of fast ( $|v_i| > 1000 \text{ m/s}$ ) inhomogeneous flows, enhanced  $T_e$  and  $T_i$ , and where the observed density has significantly decreased, i.e., consistent with the poleward flow motion observed by SuperDARN and the TEC maps shown in Figure 2 a3 and a4. It is worth mentioning that no scintillation are observed on the equatorward part of the trough (on the boundary with the low latitude solar EUV).

To further highlight the presence of small-scale plasma density structures, Figure 5 shows the spectral widths obtained from SuperDARN, which provide backscatter from decameter-scale irregularities (Chisham et al., 2007). The times and the layout are sim-

ilar to ones shown in Figure 1, i.e. geomagnetic North  $(N_m)$  is on top, the red box illustrates the region with strongest phase scintillation, and the black line the ESR field-of-view. In the beginning of the event, i.e. before the flow channel, the spectral width is low in the ESR field-of-view, as can be seen in Figure 5 a). In panel b), which corresponds to the time interval during which the convection reversed and the narrow channel appeared, an increase in the spectral width can be observed in the middle and northern part of the of the ESR field of view. Figure 5 c), shows the spectral width for the time interval including the onset and largest phase scintillation levels. Large values of spectral width (225 m/s) are seen to coincide with the region of strongest scintillation, as highlighted by the red box. In panel d), the spectral width decreases in the ESR field-of-view, but is still enhanced compared to the beginning of the event (panel a)).



**Figure 5.** SuperDARN spectral width derived by combining data from the Hankasalmi and Pykkvibaer radars on a grid and integrated over 6 minutes. Coordinates are AACGM with MLTs shown on the top of each panel. The fan shape illustrates the ESR field of view and the red box the region with largest phase scintillation indices.

Before discussing the observations, we briefly summarize the observations leading to enhanced phase scintillations. The event started with a preexisting southward-moving broad region of enhanced density poleward of a density trough, with representative values of about  $4\cdot 10^{11}~m^{-3}$  and  $1\cdot 2\cdot 10^{11}~m^{-3}$ , respectively (Figure 3 scans  $\mathbf{S_0}\cdot\mathbf{S_3}$ ). The large-scale flow reversed and a meso-scale channel of enhanced convection near the boundary between the high and low density plasmas appeared with median velocities reaching 700-900 m/s inside and about -100~m/s to -500~m/s outside of the channel (Figure 1 and 3 scans  $\mathbf{S_1}\cdot\mathbf{S_3}$ ). This implies maximum total velocity differences between the flow channel and its surrounding reaching about  $\Delta V \approx 1400~\text{m/s}$  (over several radar beams). It is worth mentioning that DMSP observed even higher velocities in the flow

channel. Furthermore, enhanced  $T_e$  likely due to fine-structured low-energy particle precipitation and a broader poleward motion of about 500 m/s are then visible in Scan  $S_2$ .

#### 4 Discussion of the observations

476

477

478

479

482

483

484

485

486

490

491

495

496

497

498

501

502

503

505

506

510

511

512

513

514

515

516

517

518

519

520

521

523

524

525

At high latitudes, enhanced density irregularities and large phase scintillations generally peak in the cusp and in the auroral oval, regions known to be ionospheric footprints of the coupling between the solar wind and magnetosphere (Prikryl et al., 2015; Jin et al., 2015, 2019). Inhomogeneous flows being common features due to this coupling (e.g. Southwood, 1987; Pinnock et al., 1993; Basu et al., 1994; Clauer, 2003; Oksavik et al., 2004b; Heppner et al., 1993; Rinne et al., 2007), we investigated the concurrence of enhanced scintillation indices and a narrow channel of intensified convection with flow shears on its flanks including an RFE. Previous studies noted the presence of small-scales plasma irregularities (e.g. Oksavik et al., 2011; Spicher et al., 2016), moderate phase scintillation ( $\sigma_{\phi} < 0.3$  rad) and low amplitude scintillation (Jin et al., 2017, 2019b) in relation to RFEs. Here, we present an evidence that strong phase scintillation indices ( $\sigma_{\phi} > 0.5$  rad) can arise from such events.

The event started with a preexisting broad region of enhanced density at high latitudes poleward of a density trough, a scenario different to the more typical case related to polar cap patch formation from the low latitude solar EUV plasma (e.g. Jin et al., 2017; Carlson, 2012, end references therein) or directly from auroral precipitation (Oksavik et al., 2006). The strongest phase scintillation and enhanced spectral width observed within the field of view of ESR arose thus shortly after a reconfiguration of the ionospheric convection on the poleward side of a narrow cusp flow channel, supporting that magnetosphereionosphere coupling is an important element in the generation of small-scale plasma irregularities and scintillation in the cusp (e.g. Prikryl et al., 2015; Jin et al., 2017). The onset of enhanced scintillations coincided with the presence of sheared (reversed) plasma flows and fine-structured low-energy particle precipitation at the boundary between the high density reservoir and the low density trough. No enhanced scintillation indices were detected on the equatorward side of the flow channel in the trough, even though fast sheared flows (with values as high as on the poleward side) and large  $T_e$  were apparent in that low-density region. Having preexisting high density such as the high-latitude plasma reservoir in our case appears thus to be a crucial component for the onset of enhanced scintillation. One plausible explanation for the higher scintillation level we observe compared to one associated with the RFE in Jin et al. (2019b) could indeed be related to the presence of the high-density region in our case. The latter RFE was characterized by conditions (flow shears, temperatures, densities and vTEC) fairly similar to the ones we measure in our trough. Our observations reinforce the suggestions from Jin et al. (2015, 2017) that the combination of high density regions (polar cap patches in their case) and auroral dynamics create stronger scintillations than only auroral dynamics.

Recent modelling work was performed to study the effect of GDI on navigation signals (K. B. Deshpande & Zettergren, 2019) and here, as we observe inhomogeneous flows near the boundary between a density reservoir and a trough, we focus essentially on the KHI as a primary mechanism. We perform numerical simulations of the KHI and investigate in more detail the plausibility for it to generate density irregularities and associated phase scintillations in the cusp ionosphere.

## 5 Numerical simulations

In the following, we present a quantitative, nonlinear analysis of KHI using numerical simulations from GEMINI-SIGMA. We use typical winter conditions and an initial configuration similar to the one leading to the strongest phase variations observed, i.e., high and low density plasma regions separated by a flow shear, as shown in Figure 3 scans S2-S3. These simulations are computationally expensive (taking several days with hun-

dreds of processors) so we take the approach of running the simulation with representative values for our event rather than running through all reasonable combinations of input parameters. This modeling effort is, thus, not a parametric study but more of a demonstration of the feasibility of KHI as an agent to produce scintillation under similar situations.

526

527

530

531

532

533

535

536

537

539

540

541

542

543

544

548

549

550

551

552

553

555

556

560

561

562

563

564

567

568

572

573

574

The initial conditions needed to set up the KHI scenario, starting from an equilibrium ionosphere are discussed in detail in Keskinen et al. (1988). This equilibrium prescribes definite relations between the velocity and density fields, such that initial Pedersen current divergences are zero. Here, we use initial conditions emphasizing the anticorrelation between high density and high flow regions seen in the ESR scan which take the form:

$$n_{e}(x, y, z, t_{0}) = n_{e0}(z) + n_{e1}(z) \left[ \frac{1}{2} + \frac{1}{2} \tanh \left( \frac{y}{\ell} \right) \right]$$

$$v_{x}(x, y, z, t_{0}) = v_{0} + v_{1} \left[ \frac{1}{2} - \frac{1}{2} \tanh \left( \frac{y}{\ell} \right) \right],$$
(2)

$$v_x(x, y, z, t_0) = v_0 + v_1 \left[ \frac{1}{2} - \frac{1}{2} \tanh\left(\frac{y}{\ell}\right) \right], \qquad (2)$$

where  $v_0$  and  $v_1$  are the flow values perpendicular to the magnetic field on each side of the shear,  $n_{e0}$  is the background density,  $n_{e1}$  is the maximum density, and  $\ell$  corresponds to the scale size of the initial shear. It is not completely possible to constrain the scale size  $\ell$  in the model as none of the measurements resolve the scales necessary to capture the fastest growing modes (e.g. DMSP samples are at 1 s, implying about 8 km resolution, ESR resolution is considerably larger). Thus, for this modeling study we choose a somewhat arbitrary scale length  $\ell=1$  km on the initial density and shear to emphasize the plausible situation where irregularities develop in a time frame similar to what is observed, while we use values consistent with the ESR observations to constrain the flow and density values. The drift velocities are taken to be  $v_0 \approx 0.1$  km/s and  $v_1 \approx$ 1.2 km/s, and the density parameters  $n_{e0} = 1 \cdot 10^{11} \text{ m}^{-3}$  and  $n_{e1} = 4.5 \cdot 10^{11} \text{ m}^{-3}$ . A small amount of additive noise is included in the initial conditions in order to seed the instability.

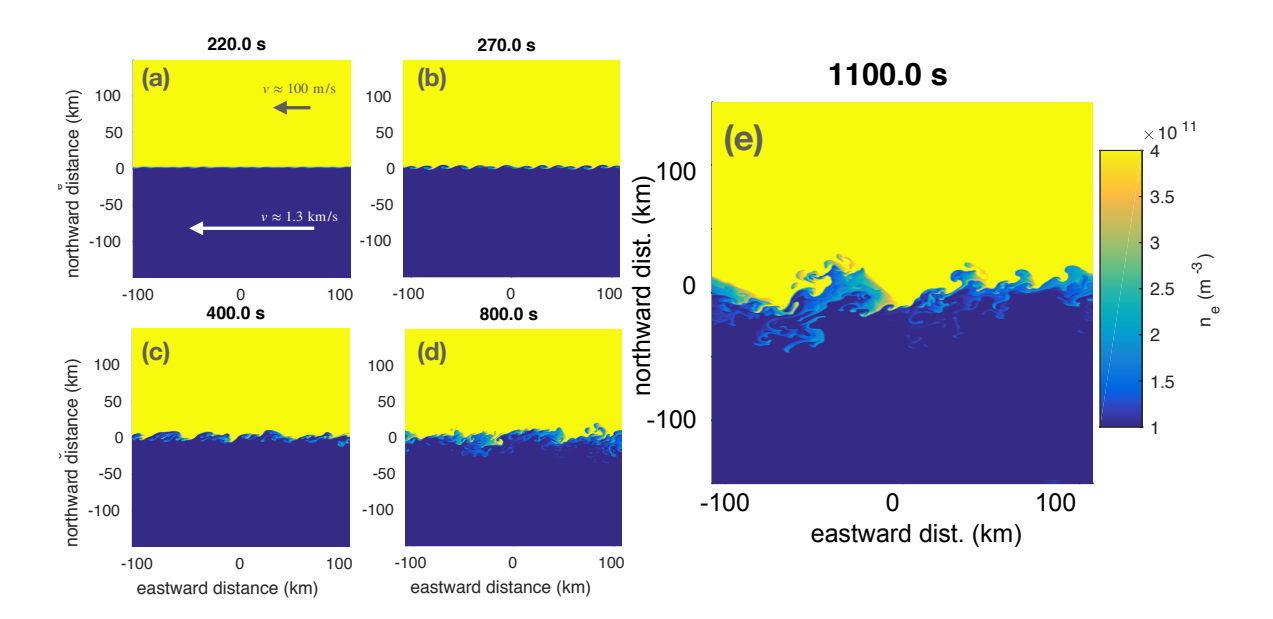
The development of KHI in the ionosphere depends on a number of parameters including: (1) inertial capacitance to conductance ratio, (2) Hall conductance (3), background velocity and shear, (4) background density and density jump, and (5) shear transition scale length. As discussed in detail in Keskinen et al. (1988), the inertial capacitance to conductance ratio determines, to a degree, the growth rates of KHI and the general behavior of the instability in the nonlinear regime. KHI is triggered by polarization currents in the ionosphere-magnetosphere system, and can be damped by a nonzero Pedersen conductance, which shorting of the instability through conduction currents flowing in the F-region. Pedersen effects also cause the nonlinear stages of the instability to progress differently, generally leading to more wave breaking and somewhat different spectrum of irregularities (Keskinen et al., 1988). It is not possible to completely cover this parameter space for the present study due to the time cost of running our models; hence, we fix the transition scale length at 1 km and perform two simulations having different values for inertial capacitance. The maximum Pedersen conductance over the grid for each run is  $\sim 1.2$  S, and the maximum inertial capacitances used in the simulations are  $\sim 10$  F (case B), and  $\sim 30$  F (case C). These values are within typical ranges cited in limited available KHI modeling literature (Keskinen et al., 1988; Huba et al., 1988).

Modeled evolution of KHI from GEMINI (Zettergren et al., 2015) is shown in Figure 6 at five different times illustrating development of the irregularities for the case B simulation (10 F inertial capacitance). The panels of this figure show density at 300 km altitude vs. eastward and northward distance. A movie showing the entire simulated density in all three dimensions is given in the supporting material for this article (Movie S1). Figure 6 (a) shows the model density following 220 s of evolution - the high density reservoir and the low density region are shown in yellow and blue, respectively. Barely visible waves seem growing in the boundary layer; otherwise the simulated conditions are

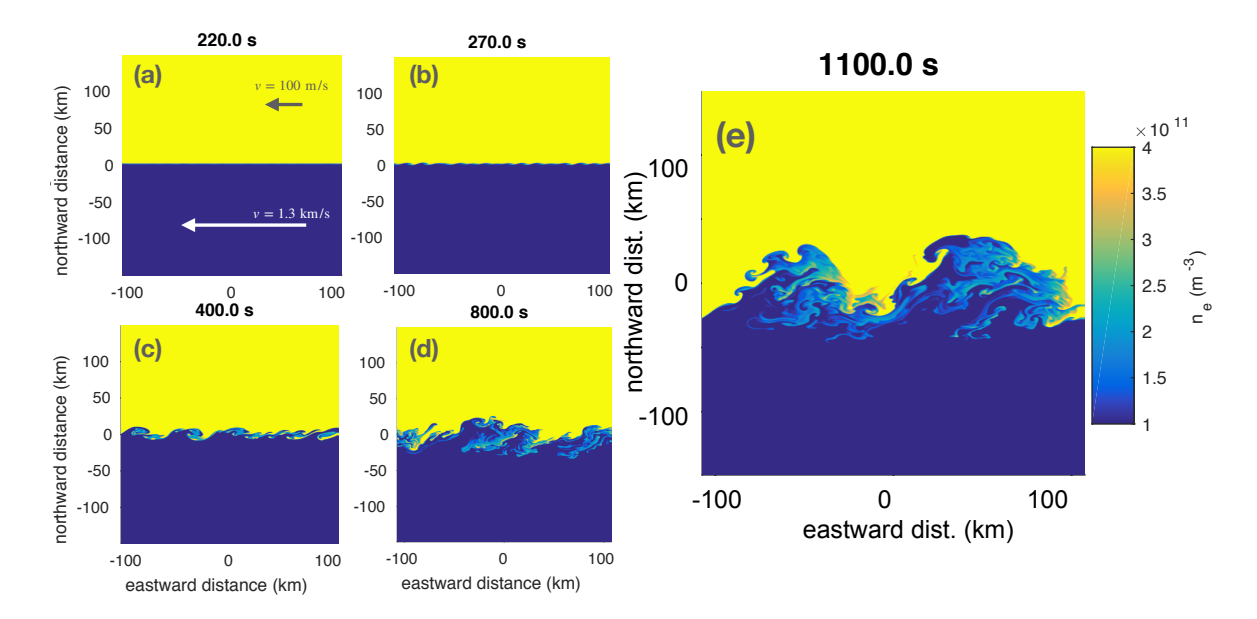
representative of the initially imposed state (from Figure 3). After about 270 s into the simulation, vortices characteristic of KHI have formed in the boundary layer; by 400 s these vortices have begun to merge, while Pedersen current effects, manifesting as the appearance of breaking waves, are clearly present (c.f. Keskinen et al., 1988). Later stage evolution of the instability that we have simulated shows a rich spectrum of irregularity features (panels d-e), including smaller-scale irregularities of the type that would be expected to impact ionospheric radio propagation. These turbulent features exhibit strong evidence of secondary instability. This includes apparently partially formed secondary vortices growing on the primary instability (these also tend to break, likely due to Pedersen effects) and also some suggestion of secondary GDI (e.g. distorted bubble-like regions of sharp discontinuity in density in panels e).

Figure 7 shows the same initial condition but run with an inertial capacitance of 30 F (case C). As compared to case B, this run exhibits more vortex merging (panel c), and larger vortices in the nonlinear stage (panel e), along with what appears to be bubble-like features (panel e) reminiscent of secondary GDI. The three dimensional movie is also given in the supporting material (Movie S2).

The numerical simulations presented in Figures 6 and 7 show that density structures can be created relatively fast ( $\sim$  minutes) through the KHI using a shear scale length of  $\ell=1$  km. This time range is well contained within the time interval during which ESR observed the sheared flow (Figure 3 Scans  $S_1$  to  $S_3$ ), making KHI a plausible primary candidate for the creation of the perturbations observed. It is also worth noting that the initial densities used for the simulations are smooth. Density structures may appear even faster for a realistic case where the density is not uniform to start with. On the other hand, increasing the scale length of the velocity gradient will generally increase the growth rate and increase the wavelength of the fastest growing mode.



**Figure 6.** Snapshots from simulations case B showing the electron density from GEMINI at 300 km altitude at different times during the development of the simulated Kelvin-Helmholtz instability.



**Figure 7.** Snapshots from simulation case C showing the electron density from GEMINI at 300 km altitude at different times during the development of the simulated Kelvin-Helmholtz instability.

We then propagate GPS L1 signal through the ionospheric structures obtained from GEMINI using the SIGMA model (Deshpande et al., 2014; K. B. Deshpande & Zettergren, 2019). Estimating a precise KHI onset time is not straightforward, but our observations suggest that enhanced phase scintillations appear within about 3-6 minutes after the beginning of the flow channel event, maximize around 6-10 min, and last for about 20 minutes. Thus, we performed the analysis on three intervals of about 60 s to 120 s long at different stages of the development of KHI. We did our simulations at 3 minutes, 9 minutes and 16 minutes into the KHI development for GEMINI runs (cases B and C). As expected at high latitudes and consistent with our observations, our simulations yielded phase scintillations predominantly. Figure 8 shows 2D snapshots from the GEMINI (case B) KHI movie of electron number density as the KHI evolves and their respective 2D propagated phases on ground through SIGMA (case C is shown in the supplementary material Figures S5). Note that the high density plasma exists on the poleward (northern) side. Detrended phase time series at the bottom panel of the figure is derived from the phase values taken at the receiver's location depicted by red crosses in figure 8.

Notable phase variations can be observed in the middle and late stage of the simulations for case B, and C, respectively, suggesting it to be slower than expected from the observations.

We also noticed in our simulations that the scintillations are stronger when either the ray path goes through the "steep" density gradients of the vortices (or simply the boundary between large density-low density in the beginning). We appear to have more small scale structures riding on the density gradients or both. For example, phase scintillations tend to strengthen when larger vortices appear to enter or exit through the ray path for the GNSS signal at 990 s and 1035 s. Scintillations weaken when the ray path is in the middle of the larger vortices or earlier in the development of the instability without much smaller scale structures developed. The phase variations obtained from SIGMA reach maxima of about  $\pm 0.4$  rad in Case B and C, which is about 1/3 of the maxima obtained from the real GPS data (see additional material Figure S4 G28). We have seen

that high flow velocities contribute to faster, stronger and more frequent scintillations (initial results from a case with faster flows, not shown and left for future work).

We envisage several possibilities to explain the difference between the model and observations. This includes (a) the contribution from other mechanisms (e.g., we don't attempt to model the precipitation), (b) underestimates of the flow values used in the model (DMSP observes much faster velocities than the field-of-view ESR ones, and initial simulations results with faster velocity of about 2 km/s increase the scintillation levels), (c) insufficient consideration of velocity filter effects (e.g. Wang et al., 2018), (d) difficulties to constrain the model to simulate the exact event (e.g. the use of smooth initial conditions, uncertainties related to the scale length of the shear and the magnetospheric influence part, which is encapsulated in the inertial capacitance), and (5) limited resources to perform an inverse analysis to find the best fit of the GEMINI-SIGMA model output to the observations. This is because combined runs of over a thousand times would be expected for such an analysis and just 1 such run takes few days if not a few weeks on a high end computer.

One must indeed note that simulations included in this study are performed using a specific set of parameters supported by the data; yet there are many adjustable parameters that *cannot* be fully constrained (e.g. scale length, and inertial capacitance). Additionally, there is a quite large parameter space to explore for fully characterizing nonlinear-stage KHI behavior. Nevertheless, the simulations show that significant density irregularities and phase variations (and thus,  $\sigma_{\phi}$ ) can arise from such a representative case of sheared-flow, supporting that KHI is likely significantly contributing in situations similar to the one presented, provided short gradient length-scales.

Previous studies (Rinne et al., 2007; Oksavik et al., 2011) have identified that RFEs were regular features of the cusp, generally most frequent for IMF  $|B_y| > |B_z|$ , i.e. when IMF is dominated by  $B_y$  (as it is the case for the current study). KHI may thus also be a common feature of the cusp, and a question arising is whether there are any particular conditions in the solar wind that may give preference to, for example, KHI over GDI. Indeed, it suggests that IMF  $B_y$  can potentially play an important role for when flow shears form in the cusp and, consequently, when the KHI mechanism is most likely to operate. However, it needs to be investigated further in future studies whether different mechanisms (e.g. KHI and GDI or a certain combination of both) actually dominate under different solar wind conditions.

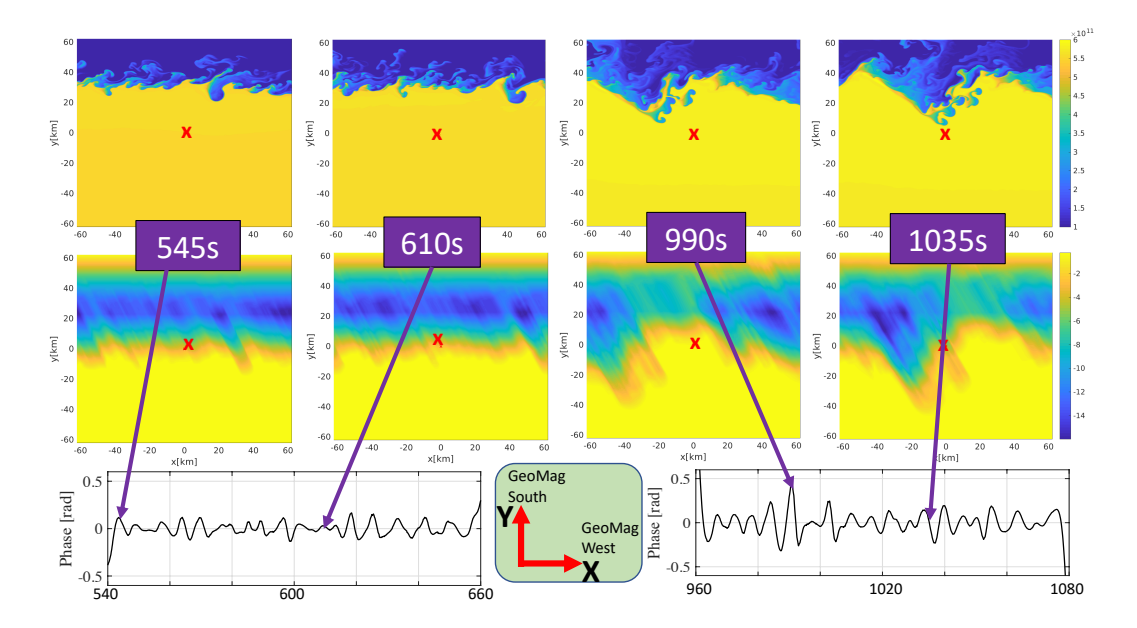


Figure 8. Snapshots from a SIGMA simulation depicting (top row) the 2D number density  $(\cdot 10^{11} \text{ electrons/m}^3)$  from GEMINI run case B at the height of maximum F2, (middle row) the 2D phase in radians projected on the ground through SIGMA, and (bottom row), the resulting SIGMA phase time series showing scintillation at different stages as the KHI is operating. Inset shows the X-Y directions for the 2D plots in the upper two rows.

## 6 Conclusion

We presented observations of a narrow cusp flow channel and RFE, i.e., exemplary multi-scale phenomena: They result from magnetosphere-ionosphere coupling, are embedded in a larger scale flow pattern and involve structures ranging from several kilometers to tens of meters. We provided evidence that strong phase scintillation ( $\sigma_{\phi} > 0.5 \text{ rad}$ ) could arise from such events, confirming that they are important in the context of impacts of space weather on technology. We compared in more detail different sources of free energy observed through 2D maps of density, velocity and temperatures, obtained from the scanning capabilities of ESR, with scintillation indices detected from a network of four GNSS receivers around Svalbard. We found that the strongest phase scintillation coincided with enhanced SuperDARN spectral width and were localized on the poleward side of the flow channel, in a region of sheared flow with structured low-energy particle precipitation. Furthermore, the presence of enhanced electron density appeared to be a prerequisite for the strongest scintillation to arise.

Observations were placed in context of the KHI due to velocity shear observations and the prevalence of inhomogeneous flows near the cusp (e.g. Heppner et al., 1993; Oksavik et al., 2004b, 2005; Carlson et al., 2008; Rinne et al., 2007; Moen et al., 2008), where phase scintillations peak (Prikryl et al., 2015; Jin et al., 2015, 2017). We do not rule out GDI or precipitation (or alternative possibilities) as playing a role in the scintillation for the specific event. Instead, we showed that, under reasonable assumptions consistent with the data, KHI can relatively easily explain the creation of density irregularities within minutes. KHI is thus likely under conditions similar to the ones observed, which are common in the cusp (Rinne et al., 2007; Oksavik et al., 2011). This is the case even with considerations for Hall currents and recombination, which are included in our model but not the original KHI modeling study of Keskinen et al. (1988). Thus, we have performed the

first quantitative, nonlinear analysis suggesting KHI as a process involved in the irregularity generation in the cusp.

Finally, this study shows that wide field-of-view incoherent scatter radar experiments (e.g., our ESR fast azimuth sweeps, or future volumetric measurements with EIS-CAT3D (McCrea et al., 2015) have great potential for investigating space weather phenomena in the ionosphere. It also illustrates some of the capabilities of GEMINI-SIGMA modeling for future parametric studies to constrain KHI and to compare its relative importance with respect to concurrent mechanisms (e.g. GDI, precipitation etc.). This study has certainly demonstrated that compared to GDI, KHI displays a specific pattern in scintillation occurrence, that is, with respect to the density boundaries, vortices and small scale structures developing around those vortices.

Future modeling work will need to focus more on how KHI develops in the nonlinear stage in situations representative of different boundary layer widths ( $\ell$ ) and different levels of ion-neutral and ionospheric-magnetospheric coupling. An assessment of how these density irregularities manifest as different scintillation signatures will also be revealing. The type of seeding used to trigger the instability will also affect the character of the response, viz. we use white noise to seed the simulations, while Keskinen et al. (1988) use single modes (eigenfunctions) to seed their instability. In particular, we identify the need to examine realistic initial conditions (nonuniform density and velocity) and structured particle precipitation as a seed process for KHI and related instabilities (e.g. Moen et al., 2012; Oksavik et al., 2012), and develop mixed-mode examples of simulations.

Observationally, it is necessary, moving forward, to quantify the scale lengths present in RFEs and other ionospheric shear flow events with high-resolution instruments. These are of importance to understanding cusp scintillation and greatly impact our simulation results. Additionally, a better statistical characterization of conditions accompanying sheared flows (precipitation, typical velocities and shears) will also help inform and constrain parameter modeling efforts to understand the relation of KHI to scintillation in the cusp.

## Acknowledgments

686

687

688

689

690

691

692

695

696

697

699

700

701

702

703

707

708

709

711

712

713

714

715

716

718

719

720

721

722

723

726

727

728

729

730

731

733

734

735

This research is part of the 4DSpace Strategic Research Initiative at University of Oslo. The Research Council of Norway has provided financial support to AS, JM (grant 275653), and KO (grants 212014 and 223252), and LBNC and YJ (grant 235655). KD's work on investigating scintillation through KHI structures was supported by NSF CA-REER grant AGS-1848207. The work by MH was supported by NASA grant NNX15AT31G. EISCAT is an international association supported by research organizations in China (CRIRP), Finland (SA), Japan (NIPR and STEL), Norway (NFR), Sweden (VR), and the United Kingdom (NERC). Data from EISCAT can be obtained from the Madrigal database https:// portal.eiscat.se/madrigal/. GPS TEC data products and access through the Madrigal distributed data system are provided to the community (http://www.openmadrigal.org) by the Massachusetts Institute of Technology (MIT) under support from US National Science Foundation grant AGS-1242204. Data for TEC processing is provided from the following organizations: UNAVCO, Scripps Orbit and Permanent Array Center, Institut Geographique National, France, International GNSS Service, The Crustal Dynamics Data Information System (CDDIS), National Geodetic Survey, Instituto Brasileiro de Geografia e Estatística, RAMSAC CORS of Instituto Geográfico Nacional de la República Argentina, Arecibo Observatory, Low-Latitude Ionospheric Sensor Network (LISN), Topcon Positioning Systems, Inc., Canadian High Arctic Ionospheric Network, Centro di Ricerche Sismologiche, Système d'Observation du Niveau des Eaux Littorales (SONEL), RENAG : REseau NAtional GPS permanent, GeoNet - the official source of geological hazard information for New Zealand, GNSS Reference Networks, Finnish Meteorological Institute, and SWEPOS - Sweden. Access to these data is provided by madrigal network via: http://

```
cedar.openmadrigal.org/. GEMINI is free, open-source software and can be down-
737
      loaded from GitHub at https://github.com/gemini3d/. Build instructions, example
738
      simulations, and documentation are also included on this website. Development of GEM-
      INI was supported under NSF CAREER grant AGS-1255181. Movies of the GEMINI
      simulations shown in the figures are included in the supporting information while the
741
      GNSS data (Oksavik et al., 2020), the GEMINI code release used for this manuscript,
742
      incl. GEMINI (Hirsch et al., 2020), GEMINI-scripts (Zettergren & Hirsch, 2020c), GEMINI-
743
      examples (Zettergren & Hirsch, 2020b), GEMINI-docs (Zettergren & Hirsch, 2020a), and
744
      the outputs from the GEMINI-SIGMA combination (K. Deshpande et al., 2020) are placed
745
      in repositories. MZ and KD gratefully acknowledge use of the ERAU Vega High-Performance
746
      Computing Cluster for running simulations presented in this paper. MZ would like to
      thank Dr. Michael Hirsch for guidance in how to set up an archive DOIs with connec-
      tions to GitHub. The authors acknowledge the use of SuperDARN data. SuperDARN
749
      is a collection of radars funded by national scientific funding agencies of Australia, Canada,
750
      China, France, Japan, South Africa, United Kingdom and United States of America. The
751
      OMNI solar wind data, the DMSP SSJ 5, and the SSIES data are provided through NASA's
      Space Physics Data Facility (SPDF) (https://cdaweb.gsfc.nasa.gov/index.html/. DMSP
753
      SSJ data can also be accessed at the National Oceanic and Atmospheric Administration
754
      (NOAA) National Centers for Environmental Information (NCEI) (https://www.ngdc.noaa.gov/stp/satellite/dms
      Finally, the authors gratefully acknowledge the helpful comments from the reviewers.
```

## References

757

758

759

762

763

765

768

769

770

771

772

774

775

776

777

778

780

781

782

783

784

787

- Alfonsi, L., Spogli, L., Tong, J., Franceschi, G. D., Romano, V., Bourdillon, A., ... Mitchell, C. (2011). GPS scintillation and TEC gradients at equatorial latitudes in April 2006. Advances in Space Research, 47(10), 1750 1757. (GNSS Remote Sensing-2) doi: https://doi.org/10.1016/j.asr.2010.04.020
- Baker, K. B., & Wing, S. (1989). A new magnetic coordinate system for conjugate studies at high latitudes. *Journal of Geophysical Research: Space Physics*, 94(A7), 9139-9143. doi: 10.1029/JA094iA07p09139
- Basu, S., Basu, S., Chaturvedi, P. K., & Bryant Jr., C. M. (1994). Irregularity structures in the cusp/cleft and polar cap regions. Radio Science, 29(1), 195-207. doi: 10.1029/93RS01515
- Basu, S., Basu, S., MacKenzie, E., Fougere, P. F., Coley, W. R., Maynard, N. C., ... Hoegy, W. R. (1988). Simultaneous density and electric field fluctuation spectra associated with velocity shears in the auroral oval. *Journal of Geophysical Research: Space Physics*, 93(A1), 115-136. doi: 10.1029/JA093iA01p00115
- Basu, S., Basu, S., Senior, C., Weimer, D., Nielsen, E., & Fougere, P. F. (1986). Velocity shears and sub-km scale irregularities in the nighttime auroral F-region. Geophysical Research Letters, 13(2), 101-104. doi: 10.1029/GL013i002p00101
- Beach, T. L. (2006). Perils of the GPS phase scintillation index ( $\sigma_{\phi}$ ). Radio Science, 41(5). doi: 10.1029/2005RS003356
- Blelly, P., & Schunk, R. (1993). A comparative study of the time-dependent standard 8-, 13- and 16-moment transport formulations of the polar wind. In Annales geophysicae (Vol. 11, pp. 443–469).
- Briggs, B., & Parkin, I. (1963). On the variation of radio star and satellite scintillations with zenith angle. *Journal of Atmospheric and Terrestrial Physics*, 25(6), 339 366. doi: https://doi.org/10.1016/0021-9169(63)90150-8
- Cargill, P. J., Lavraud, B., Owen, C. J., Grison, B., Dunlop, M. W., Cornilleau-Wehrlin, N., . . . Nykyri, K. (2005). Cluster at the Magnetospheric Cusps. In G. Paschmann, S. J. Schwartz, C. P. Escoubet, & S. Haaland (Eds.), Outer Magnetospheric Boundaries: Cluster Results (pp. 321–366). Dordrecht: Springer Netherlands. doi: 10.1007/1-4020-4582-4\$\\_\$10
- Carlson, H. C. (2012). Sharpening our thinking about polar cap ionospheric patch morphology, research, and mitigation techniques. *Radio Science*, 47(4). doi: 10

.1029/2011RS004946

- Carlson, H. C., Oksavik, K., & Moen, J. (2008). On a new process for cusp irregularity production. *Annales Geophysicae*, 26(9), 2871–2885. doi: 10.5194/angeo -26-2871-2008
- Carlson, H. C., Oksavik, K., Moen, J., van Eyken, A. P., & Guio, P. (2002). ESR mapping of polar-cap patches in the dark cusp. Geophysical Research Letters, 29(10), 24-1-24-4. doi: 10.1029/2001GL014087
- Carlson, H. C., Pedersen, T., Basu, S., Keskinen, M., & Moen, J. (2007). Case for a new process, not mechanism, for cusp irregularity production. *Journal of Geo*physical Research: Space Physics, 112(A11). doi: 10.1029/2007JA012384
- Chaston, C. C., Carlson, C. W., McFadden, J. P., Ergun, R. E., & Strangeway, R. J. (2007). How important are dispersive Alfvén waves for auroral particle acceleration? Geophysical Research Letters, 34 (7). doi: 10.1029/2006GL029144
- Chisham, G., Lester, M., Milan, S. E., Freeman, M. P., Bristow, W. A., Grocott, A., ... Walker, A. D. M. (2007). A decade of the Super Dual Auroral Radar Network (SuperDARN): scientific achievements, new techniques and future directions. Surveys in Geophysics, 28(1), 33–109. doi: 10.1007/s10712-007-9017-8
- Clauer, C. R. (2003). Ionospheric observations of waves at the inner edge of the low latitude boundary layer. In *Earth's low-latitude boundary layer* (p. 297-309). American Geophysical Union (AGU). doi: 10.1029/133GM30
- Clausen, L. B. N., Moen, J. I., Hosokawa, K., & Holmes, J. M. (2016). GPS scintillations in the high latitudes during periods of dayside and nightside reconnection. *Journal of Geophysical Research: Space Physics*, 121(4), 3293-3309. doi: 10.1002/2015JA022199
- Deshpande, K., Spicher, A., Jin, Y., Oksavik, K., Zettergren, M. D., Clausen, L. B. N., . . . Baddeley, L. J. (2020). GEMINI-SIGMA output Replication Data for: "On the production of ionospheric irregularities via Kelvin-Helmholtz instability associated with cusp flow channels". DataverseNO. doi: 10.18710/5IYSKV
- Deshpande, K. B., Bust, G. S., Clauer, C. R., Rino, C. L., & Carrano, C. S. (2014). Satellite-beacon Ionospheric-scintillation Global Model of the upper Atmosphere (SIGMA) I: High latitude sensitivity study of the model parameters. Journal of Geophysical Research: Space Physics, 119, 4026-4043. doi: 10.1002/2013JA019699
- Deshpande, K. B., & Zettergren, M. D. (2019). Satellite-Beacon Ionospheric-Scintillation Global Model of the Upper Atmosphere (SIGMA) III: Scintillation Simulation Using A Physics-Based Plasma Model. Geophysical Research Letters, 46(9), 4564-4572. doi: 10.1029/2019GL082576
- Diloy, P.-Y., Robineau, A., Lilensten, J., Blelly, P.-L., & Fontanari, J. (1996). A numerical model of the ionosphere, including the E-region above EISCAT. In *Annales geophysicae* (Vol. 14, pp. 191–200).
- Doe, R. A., Kelly, J. D., & Sánchez, E. R. (2001). Observations of persistent dayside F region electron temperature enhancements associated with soft magnetosheathlike precipitation. *Journal of Geophysical Research: Space Physics*, 106(A3), 3615-3630. doi: 10.1029/2000JA000186
- Dyson, P. L., & Winningham, J. D. (1974). Top side ionospheric spread F and particle precipitation in the day side magnetospheric clefts. *Journal of Geophysical Research* (1896-1977), 79 (34), 5219-5230. doi: 10.1029/JA079i034p05219
- Earle, G. D., Kelley, M. C., & Ganguli, G. (1989). Large velocity shears and associated electrostatic waves and turbulence in the auroral F region. *Journal of Geophysical Research: Space Physics*, 94 (A11), 15321-15333. doi: 10.1029/JA094iA11p15321
- Fang, X., Randall, C. E., Lummerzheim, D., Solomon, S. C., Mills, M. J., Marsh,
  D. R., . . . Lu, G. (2008). Electron impact ionization: A new parameterization for 100 eV to 1 MeV electrons. *Journal of Geophysical Research: Space*

Physics, 113(A9).

- Forsythe, V. V., & Makarevich, R. A. (2018). Statistical Analysis of the Electron Density Gradients in the Polar Cap F Region Using the Resolute Bay Incoherent Scatter Radar North. *Journal of Geophysical Research: Space Physics*, 123(5), 4066-4079. doi: 10.1029/2017JA025156
- Forte, B., Coleman, C., Skone, S., Häggström, I., Mitchell, C., Da Dalt, F., ... Bust, G. (2017). Identification of scintillation signatures on GPS signals originating from plasma structures detected with EISCAT incoherent scatter radar along the same line of sight. *Journal of Geophysical Research: Space Physics*, 122(1), 916-931. doi: 10.1002/2016JA023271
- Forte, B., & Radicella, S. M. (2002). Problems in data treatment for ionospheric scintillation measurements. Radio Science, 37(6), 8-1-8-5. doi: 10.1029/2001 RS002508
- Fremouw, E. J., Leadabrand, R. L., Livingston, R. C., Cousins, M. D., Rino, C. L., Fair, B. C., & Long, R. A. (1978). Early results from the DNA Wideband satellite experiment—Complex-signal scintillation. Radio Science, 13(1), 167-187. doi: 10.1029/RS013i001p00167
- Ganguli, G., Keskinen, M. J., Romero, H., Heelis, R., Moore, T., & Pollock, C.
   (1994). Coupling of microprocesses and macroprocesses due to velocity shear:
   An application to the low-altitude ionosphere. Journal of Geophysical Research: Space Physics, 99(A5), 8873-8889. doi: 10.1029/93JA03181
- Gondarenko, N. A., & Guzdar, P. N. (2004). Plasma patch structuring by the nonlinear evolution of the gradient drift instability in the high-latitude ionosphere. *Journal of Geophysical Research: Space Physics*, 109 (A9). doi: 10.1029/2004JA010504
- Hairston, M. (2019). A Short Introduction to the DMSP SSIES-3 Quality Flags and How to Use Them. SPDF technical document. Retrieved from https://spdf.gsfc.nasa.gov/pub/data/dmsp/documents/ssies/SSIES-3\_qualityflags\_Sept2019.pdf
- Hardy, D. A., Holeman, E. G., Burke, W. J., Gentile, L. C., & Bounar, K. H. (2008). Probability distributions of electron precipitation at high magnetic latitudes. Journal of Geophysical Research: Space Physics, 113(A6). doi: 10.1029/2007JA012746
- Heppner, J. P., Liebrecht, M. C., Maynard, N. C., & Pfaff, R. F. (1993). Highlatitude distributions of plasma waves and spatial irregularities from DE 2 alternating current electric field observations. *Journal of Geophysical Research:* Space Physics, 98(A2), 1629-1652. doi: 10.1029/92JA01836
- Hey, J. S., Parsons, S. J., & Phillips, J. W. (1946, August). Fluctuations in Cosmic Radiation at Radio-Frequencies. *Nature*, 158, 234. doi: 10.1038/158234a0
- Hirsch, M., Zettergren, M. D., & Grubbs, G. (2020, February). gemini3d/GEMINI: KHI JGR version of code. Zenodo. doi: 10.5281/zenodo.3647580
- Huba, J. D., Mitchell, H. G., Keskinen, M. J., Fedder, J. A., Satyanarayana, P., & Zalesak, S. T. (1988). Simulations of plasma structure evolution in the high-latitude ionosphere. Radio Science, 23(4), 503-512. doi: 10.1029/RS023i004p00503
- Jin, Y., Miloch, W. J., Moen, J. I., & Clausen, L. B. (2018b). Solar cycle and seasonal variations of the GPS phase scintillation at high latitudes. J. Space Weather Space Clim., 8, A48. doi: 10.1051/swsc/2018034
- Jin, Y., Moen, J., & Miloch, W. J. (2014). GPS scintillation effects associated with polar cap patches and substorm auroral activity: direct comparison. J. Space Weather Space Clim., 4, A23. doi: 10.1051/swsc/2014019
- Jin, Y., Moen, J. I., & Miloch, W. J. (2015). On the collocation of the cusp aurora and the GPS phase scintillation: A statistical study. *Journal of Geophysical Research: Space Physics*, 120(10), 9176-9191. doi: 10.1002/2015JA021449
- Jin, Y., Moen, J. I., Miloch, W. J., Clausen, L. B. N., & Oksavik, K. (2016). Sta-

tistical study of the GNSS phase scintillation associated with two types of auroral blobs. Journal of Geophysical Research: Space Physics, 121(5), 4679-4697. doi: 10.1002/2016JA022613

- Jin, Y., Moen, J. I., Oksavik, K., Spicher, A., Clausen, L., & Miloch, W. J. (2017).
   GPS scintillations associated with cusp dynamics and polar cap patches. J. Space Weather Space Clim., 7, A23. doi: 10.1051/swsc/2017022
- Jin, Y., Moen, J. I., Spicher, A., Oksavik, K., Miloch, W. J., Clausen, L. B. N., ... Saito, Y. (2019b). Simultaneous Rocket and Scintillation Observations of Plasma Irregularities Associated With a Reversed Flow Event in the Cusp Ionosphere. Journal of Geophysical Research: Space Physics, 124(8), 7098-7111. doi: 10.1029/2019JA026942
- Jin, Y., Spicher, A., Xiong, C., Clausen, L. B. N., Kervalishvili, G., Stolle, C., & Miloch, W. J. (2019). Ionospheric Plasma Irregularities Characterized by the Swarm Satellites: Statistics at High Latitudes. *Journal of Geophysical Research: Space Physics*, 124(2), 1262-1282. doi: 10.1029/2018JA026063
- Kelley, M. C., & Carlson, C. W. (1977). Observations of intense velocity shear and associated electrostatic waves near an auroral arc. *Journal of Geophysical Re*search (1896-1977), 82(16), 2343-2348. doi: 10.1029/JA082i016p02343
- Kelley, M. C., Vickrey, J. F., Carlson, C. W., & Torbert, R. (1982). On the origin and spatial extent of high-latitude F region irregularities. *Journal of Geophysical Research: Space Physics*, 87(A6), 4469-4475. doi: 10.1029/JA087iA06p04469
- Keskinen, M. J., Mitchell, H. G., Fedder, J. A., Satyanarayana, P., Zalesak, S. T., & Huba, J. D. (1988). Nonlinear evolution of the Kelvin-Helmholtz instability in the high-latitude ionosphere. *Journal of Geophysical Research: Space Physics*, 93(A1), 137-152. doi: 10.1029/JA093iA01p00137
- Keskinen, M. J., & Ossakow, S. L. (1983). Theories of high-latitude ionospheric irregularities: A review. Radio Science, 18(6), 1077-1091. doi: 10.1029/RS018i006p01077
- Kilcommons, L. M., Redmon, R. J., & Knipp, D. J. (2017). A new DMSP magnetometer and auroral boundary data set and estimates of field-aligned currents in dynamic auroral boundary coordinates. *Journal of Geophysical Research:* Space Physics, 122(8), 9068-9079. doi: 10.1002/2016JA023342
- King, J. H., & Papitashvili, N. E. (2005). Solar wind spatial scales in and comparisons of hourly Wind and ACE plasma and magnetic field data. *Journal of Geophysical Research: Space Physics*, 110(A2). doi: 10.1029/2004JA010649
- Kintner, P. M., Ledvina, B. M., & de Paula, E. R. (2007). GPS and ionospheric scintillations. *Space Weather*, 5(9). doi: 10.1029/2006SW000260
- Kintner, P. M., & Seyler, C. E. (1985). The status of observations and theory of high latitude ionospheric and magnetospheric plasma turbulence. Space Science Reviews, 41(1), 91–129. doi: 10.1007/BF00241347
- Labelle, J., Sica, R. J., Kletzing, C., Earle, G. D., Kelley, M. C., Lummerzheim, D., ... Berg, G. (1989). Ionization from soft electron precipitation in the auroral F region. *Journal of Geophysical Research: Space Physics*, 94 (A4), 3791-3798. doi: 10.1029/JA094iA04p03791
- Lamarche, L. J., & Makarevich, R. A. (2017). Radar observations of density gradients, electric fields, and plasma irregularities near polar cap patches in the context of the gradient-drift instability. *Journal of Geophysical Research: Space Physics*, 122(3), 3721-3736. doi: 10.1002/2016JA023702
- Linson, L. M., & Workman, J. B. (1970). Formation of striations in ionospheric plasma clouds. *Journal of Geophysical Research (1896-1977)*, 75(16), 3211-3219. doi: 10.1029/JA075i016p03211
- Makarevich, R. A. (2014). Symmetry considerations in the two-fluid theory of the gradient drift instability in the lower ionosphere. *Journal of Geophysical Research: Space Physics*, 119(9), 7902-7913. doi: 10.1002/2014JA020292

Makarevich, R. A. (2017). Critical density gradients for small-scale plasma irregularity generation in the E and F regions. *Journal of Geophysical Research: Space Physics*, 122(9), 9588-9602. doi: 10.1002/2017JA024393

aga

- Mannucci, A. J., Wilson, B. D., & Edwards, C. D. (1993). A New Method for Monitoring the Earth's Ionospheric Total Electron Content Using the GPS Global Network. Proceedings of the 6th International Technical Meeting of the Satellite Division of The Institute of Navigation (ION GPS 1993), Salt Lake City, UT, 1323-1332.
  - McCaffrey, A. M., & Jayachandran, P. T. (2019). Determination of the Refractive Contribution to GPS Phase "Scintillation". *Journal of Geophysical Research:* Space Physics, 124(2), 1454-1469. doi: 10.1029/2018JA025759
  - McCrea, I., Aikio, A., Alfonsi, L., Belova, E., Buchert, S., Clilverd, M., ... Vierinen, J. (2015). The science case for the EISCAT\_3D radar. *Progress in Earth and Planetary Science*, 2(1), 21. doi: 10.1186/s40645-015-0051-8
  - Millward, G. H., Moffett, R. J., Balmforth, H. F., & Rodger, A. S. (1999). Modeling the ionospheric effects of ion and electron precipitation in the cusp. *Journal of Geophysical Research: Space Physics*, 104 (A11), 24603-24612. doi: 10.1029/1999JA900249
  - Mitchell, C. N., Alfonsi, L., De Franceschi, G., Lester, M., Romano, V., & Wernik, A. W. (2005). GPS TEC and scintillation measurements from the polar ionosphere during the October 2003 storm. *Geophysical Research Letters*, 32(12). doi: 10.1029/2004GL021644
  - Moen, J., Oksavik, K., Abe, T., Lester, M., Saito, Y., Bekkeng, T. A., & Jacobsen, K. S. (2012). First in-situ measurements of HF radar echoing targets. *Geophysical Research Letters*, 39(7). doi: 10.1029/2012GL051407
  - Moen, J., Oksavik, K., Alfonsi, L., Daabakk, Y., Romano, V., & Spogli, L. (2013). Space weather challenges of the polar cap ionosphere. J. Space Weather Space Clim., 3, A02. doi: 10.1051/swsc/2013025
  - Moen, J., Rinne, Y., Carlson, H. C., Oksavik, K., Fujii, R., & Opgenoorth, H. (2008). On the relationship between thin Birkeland current arcs and reversed flow channels in the winter cusp/cleft ionosphere. *Journal of Geophysical Research: Space Physics*, 113(A9). doi: 10.1029/2008JA013061
  - Moen, J., Walker, I. K., Kersley, L., & Milan, S. E. (2002). On the generation of cusp HF backscatter irregularities. *Journal of Geophysical Research: Space Physics*, 107(A4), SIA 3-1-SIA 3-5. doi: 10.1029/2001JA000111
  - Mushini, S. C., Jayachandran, P. T., Langley, R. B., MacDougall, J. W., & Pokhotelov, D. (2012). Improved amplitude- and phase-scintillation indices derived from wavelet detrended high-latitude GPS data. *GPS Solutions*, 16(3), 363–373. doi: 10.1007/s10291-011-0238-4
  - Oksavik, K., Moen, J., & Carlson, H. C. (2004a). High-resolution observations of the small-scale flow pattern associated with a poleward moving auroral form in the cusp. *Geophysical Research Letters*, 31(11). doi: 10.1029/2004GL019838
  - Oksavik, K., Moen, J., Carlson, H. C., Greenwald, R. A., Milan, S. E., Lester, M., ... Barnes, R. J. (2005). Multi-instrument mapping of the small-scale flow dynamics related to a cusp auroral transient. *Annales Geophysicae*, 23(7), 2657–2670. doi: 10.5194/angeo-23-2657-2005
  - Oksavik, K., Moen, J., Lester, M., Bekkeng, T. A., & Bekkeng, J. K. (2012). In situ measurements of plasma irregularity growth in the cusp ionosphere. *Journal of Geophysical Research: Space Physics*, 117(A11). doi: 10.1029/2012JA017835
  - Oksavik, K., Moen, J. I., Rekaa, E. H., Carlson, H. C., & Lester, M. (2011). Reversed flow events in the cusp ionosphere detected by SuperDARN HF radars. *Journal of Geophysical Research: Space Physics*, 116(A12). doi: 10.1029/2011JA016788
- Oksavik, K., Ruohoniemi, J. M., Greenwald, R. A., Baker, J. B. H., Moen, J., Carlson, H. C., . . . Lester, M. (2006). Observations of isolated polar cap patches

- by the European Incoherent Scatter (EISCAT) Svalbard and Super Dual Auroral Radar Network (SuperDARN) Finland radars. *Journal of Geophysical Research: Space Physics*, 111 (A5). doi: 10.1029/2005JA011400
- Oksavik, K., Soraas, F., Moen, J., Pfaff, R., Davies, J. A., & Lester, M. (2004b). Simultaneous optical, CUTLASS HF radar, and FAST spacecraft observations: Signatures of boundary layer processes in the cusp. *Annales Geophysicae*, 22(2), 511-525. doi: 10.5194/angeo-22-511-2004

- Oksavik, K., Spicher, A., Deshpande, K., Jin, Y., Zettergren, M. D., Clausen, L. B. N., ... Baddeley, L. J. (2020). GNSS Replication Data for: "On the production of ionospheric irregularities via Kelvin-Helmholtz instability associated with cusp flow channels". DataverseNO. doi: 10.18710/LOIWIU
- Oksavik, K., van der Meeren, C., Lorentzen, D. A., Baddeley, L. J., & Moen, J. (2015). Scintillation and loss of signal lock from poleward moving auroral forms in the cusp ionosphere. *Journal of Geophysical Research: Space Physics*, 120(10), 9161-9175. doi: 10.1002/2015JA021528
- Phelps, A. D. R., & Sagalyn, R. C. (1976). Plasma density irregularities in the highlatitude top side ionosphere. *Journal of Geophysical Research* (1896-1977), 81(4), 515-523. doi: 10.1029/JA081i004p00515
- Pinnock, M., Rodger, A. S., Dudeney, J. R., Baker, K. B., Newell, P. T., Greenwald, R. A., & Greenspan, M. E. (1993). Observations of an enhanced convection channel in the cusp ionosphere. *Journal of Geophysical Research: Space Physics*, 98(A3), 3767-3776. doi: 10.1029/92JA01382
- Prikryl, P., Jayachandran, P. T., Chadwick, R., & Kelly, T. D. (2015). Climatology of GPS phase scintillation at northern high latitudes for the period from 2008 to 2013. *Annales Geophysicae*, 33(5), 531–545. doi: 10.5194/angeo-33-531-2015
- Prikryl, P., Jayachandran, P. T., Mushini, S. C., & Chadwick, R. (2011). Climatology of GPS phase scintillation and HF radar backscatter for the high-latitude ionosphere under solar minimum conditions. *Annales Geophysicae*, 29(2), 377–392. doi: 10.5194/angeo-29-377-2011
- Redmon, R. J., Denig, W. F., Kilcommons, L. M., & Knipp, D. J.

  New DMSP database of precipitating auroral electrons and ions.

  nal of Geophysical Research: Space Physics, 122(8), 9056-9067.

  10.1002/2016JA023339

  (2017).
- Rees, M. H. (1963). Auroral ionization and excitation by incident energetic electrons. *Planetary and Space Science*, 11(10), 1209 1218. doi: https://doi.org/10.1016/0032-0633(63)90252-6
- Rich, F. J. (1994b). Users Guide for the Topside Ionospheric Plasma Monitor (SSIES, SSIES-2, and SSIES-3) on Spacecraft of the Defense Meteorological Satellite Program (DMSP). Volume I: Technical Description.

  \*Phillips Laboratory Technical Report PL-TR-94-2187.\*\* Retrieved from https://satdat.ngdc.noaa.gov/dmsp/docs/Rich-1994-UsersGuideSSIES-1SSIES-2SSIES-3-PL-TR-94-2187.pdf
- Rich, F. J., & Hairston, M. (1994). Large-scale convection patterns observed by DMSP. *Journal of Geophysical Research: Space Physics*, 99(A3), 3827-3844. doi: 10.1029/93JA03296
- Richards, P., Fennelly, J., & Torr, D. (1994). EUVAC: A solar EUV flux model for aeronomic calculations. *Journal of Geophysical Research: Space Physics*, 99(A5), 8981–8992.
- Rideout, W., & Coster, A. (2006). Automated GPS processing for global total electron content data. GPS Solutions, 10(3), 219–228. doi: 10.1007/s10291-006-0029-5
- Rinne, Y., Moen, J., Oksavik, K., & Carlson, H. C. (2007). Reversed flow events in the winter cusp ionosphere observed by the European Incoherent Scatter (EISCAT) Svalbard radar. Journal of Geophysical Research: Space Physics,

112(A10). doi: 10.1029/2007JA012366

- Rino, C. L. (1979). A power law phase screen model for ionospheric scintillation: 1. Weak scatter. Radio Science, 14(6), 1135-1145. doi: 10.1029/RS014i006p01135
- Ruohoniemi, J. M., Greenwald, R. A., Baker, K. B., Villain, J., Hanuise, C., & Kelly, J. (1989). Mapping high-latitude plasma convection with coherent HF radars. *Journal of Geophysical Research: Space Physics*, 94 (A10), 13463-13477. doi: 10.1029/JA094iA10p13463
- Schunk, R. (1977). Mathematical structure of transport equations for multispecies flows. *Reviews of Geophysics*, 15(4), 429–445.
- Semeter, J., Mrak, S., Hirsch, M., Swoboda, J., Akbari, H., Starr, G., ...
  Pankratius, V. (2017). GPS Signal Corruption by the Discrete Aurora: Precise
  Measurements From the Mahali Experiment. Geophysical Research Letters,
  44(19), 9539-9546. doi: 10.1002/2017GL073570
- Simon, A. (1963). Instability of a Partially Ionized Plasma in Crossed Electric and Magnetic Fields. *The Physics of Fluids*, 6(3), 382-388. doi: 10.1063/1.1706743
- Solomon, S. C., & Qian, L. (2005). Solar extreme-ultraviolet irradiance for general circulation models. *Journal of Geophysical Research: Space Physics*, 110 (A10).
- Southwood, D. J. (1987). The ionospheric signature of flux transfer events. *Journal of Geophysical Research: Space Physics*, 92(A4), 3207-3213. doi: 10.1029/JA092iA04p03207
- Spicher, A., Ilyasov, A. A., Miloch, W. J., Chernyshov, A. A., Clausen, L. B. N., Moen, J. I., . . . Saito, Y. (2016). Reverse flow events and small-scale effects in the cusp ionosphere. *Journal of Geophysical Research: Space Physics*, 121 (10), 10,466-10,480. doi: 10.1002/2016JA022999
- Spicher, A., Miloch, W. J., Clausen, L. B. N., & Moen, J. I. (2015). Plasma turbulence and coherent structures in the polar cap observed by the ICI-2 sounding rocket. *Journal of Geophysical Research: Space Physics*, 120(12), 10,959-10,978. doi: 10.1002/2015JA021634
- Spogli, L., Alfonsi, L., De Franceschi, G., Romano, V., Aquino, M. H. O., & Dodson, A. (2009). Climatology of GPS ionospheric scintillations over high and mid-latitude European regions. *Annales Geophysicae*, 27(9), 3429–3437. doi: 10.5194/angeo-27-3429-2009
- St-Maurice, J.-P., & Laneville, P. (1998). Reaction rate of O+ with O2, N2, and NO under highly disturbed auroral conditions. *Journal of Geophysical Research:* Space Physics, 103(A8), 17519–17521.
- Thébault, E., Finlay, C. C., Beggan, C. D., Alken, P., Aubert, J., Barrois, O., ... Zvereva, T. (2015, May 27). International geomagnetic reference field: the 12th generation. *Earth, Planets and Space*, 67(1), 79. doi: 10.1186/s40623-015-0228-9
- Thomas, E. G., Baker, J. B. H., Ruohoniemi, J. M., Clausen, L. B. N., Coster, A. J., Foster, J. C., & Erickson, P. J. (2013). Direct observations of the role of convection electric field in the formation of a polar tongue of ionization from storm enhanced density. *Journal of Geophysical Research: Space Physics*, 118(3), 1180-1189. doi: 10.1002/jgra.50116
- Tsunoda, R. T. (1988). High-latitude F region irregularities: A review and synthesis. *Reviews of Geophysics*, 26(4), 719-760. doi: 10.1029/RG026i004p00719
- Valladares, C. E., & Carlson Jr., H. C. (1991). The electrodynamic, thermal, and energetic character of intense Sun-aligned arcs in the polar cap.

  Journal of Geophysical Research: Space Physics, 96 (A2), 1379-1400. doi: 10.1029/90JA01765
- van der Meeren, C., Oksavik, K., Lorentzen, D., Moen, J. I., & Romano, V. (2014) GPS scintillation and irregularities at the front of an ionization tongue in the

- nightside polar ionosphere. Journal of Geophysical Research: Space Physics, 119 (10), 8624-8636. doi: 10.1002/2014JA020114
  - van der Meeren, C., Oksavik, K., Lorentzen, D. A., Paxton, L. J., & Clausen, L. B. N. (2016). Scintillation and irregularities from the nightside part of a Sun-aligned polar cap arc. *Journal of Geophysical Research: Space Physics*, 121(6), 5723-5736. doi: 10.1002/2016JA022708

- van der Meeren, C., Oksavik, K., Lorentzen, D. A., Rietveld, M. T., & Clausen, L. B. N. (2015). Severe and localized GNSS scintillation at the poleward edge of the nightside auroral oval during intense substorm aurora. *Journal of Geophysical Research: Space Physics*, 120(12), 10,607-10,621. doi: 10.1002/2015JA021819
- Van Dierendonck, A. J., Klobuchar, J., & Hua, Q. (1993). Ionospheric Scintillation Monitoring Using Commercial Single Frequency C/A Code Receivers. In Proceedings of the 6th international technical meeting of the satellite division of the institute of navigation (ion gps 1993) (pp. 1333–1342). Salt Lake City, UT, September 1993.
- Vierinen, J., Coster, A. J., Rideout, W. C., Erickson, P. J., & Norberg, J. (2016). Statistical framework for estimating GNSS bias. *Atmospheric Measurement Techniques*, 9(3), 1303–1312. doi: 10.5194/amt-9-1303-2016
- Vontrat-Reberac, A., Fontaine, D., Blelly, P.-L., & Galand, M. (2001). Theoretical predictions of the effect of cusp and dayside precipitation on the polar ionosphere. *Journal of Geophysical Research: Space Physics*, 106 (A12), 28857-28865. doi: 10.1029/2001JA900131
- Wang, Y., Zhang, Q.-H., Jayachandran, P. T., Lockwood, M., Zhang, S.-R., Moen, J., . . . Lester, M. (2016). A comparison between large-scale irregularities and scintillations in the polar ionosphere. *Geophysical Research Letters*, 43(10), 4790-4798. doi: 10.1002/2016GL069230
- Wang, Y., Zhang, Q.-H., Jayachandran, P. T., Moen, J., Xing, Z.-Y., Chadwick, R., ... Lester, M. (2018). Experimental Evidence on the Dependence of the Standard GPS Phase Scintillation Index on the Ionospheric Plasma Drift Around Noon Sector of the Polar Ionosphere. *Journal of Geophysical Research: Space Physics*, 123(3), 2370-2378. doi: 10.1002/2017JA024805
- Wannberg, G., Wolf, I., Vanhainen, L.-G., Koskenniemi, K., Röttger, J., Postila, M., ... Huuskonen, A. (1997). The EISCAT Svalbard radar: A case study in modern incoherent scatter radar system design. Radio Science, 32(6), 2283-2307. doi: 10.1029/97RS01803
- Weber, E. J., Buchau, J., Moore, J. G., Sharber, J. R., Livingston, R. C., Winningham, J. D., & Reinisch, B. W. (1984). F layer ionization patches in the polar cap. *Journal of Geophysical Research: Space Physics*, 89(A3), 1683-1694. doi: 10.1029/JA089iA03p01683
- Weber, E. J., Kelley, M. C., Ballenthin, J. O., Basu, S., Carlson, H. C., Fleischman, J. R., ... Smiddy, M. (1989). Rocket measurements within a polar cap arc: Plasma, particle, and electric circuit parameters. *Journal of Geophysical Research: Space Physics*, 94(A6), 6692-6712. Retrieved from https://agupubs.onlinelibrary.wiley.com/doi/abs/10.1029/JA094iA06p06692 doi: 10.1029/JA094iA06p06692
- Wernik, A., Secan, J., & Fremouw, E. (2003). Ionospheric irregularities and scintillation. *Advances in Space Research*, 31(4), 971 981. doi: https://doi.org/10.1016/S0273-1177(02)00795-0
- Yeh, K. C., & Liu, C.-H. (1982). Radio wave scintillations in the ionosphere. *Proceedings of the IEEE*, 70(4), 324-360. doi: 10.1109/PROC.1982.12313
- Zettergren, M. D., & Hirsch, M. (2020a, February). gemini3d/GEMINI-docs: KHI JGR paper. Zenodo. doi: 10.5281/zenodo.3647589
- Zettergren, M. D., & Hirsch, M. (2020b, February). gemini3d/GEMINI-examples: KHI JGR paper. Zenodo. doi: 10.5281/zenodo.3647584

- Zettergren, M. D., & Hirsch, M. (2020c, February). gemini3d/GEMINI-scripts: KHI JGR paper. Zenodo. doi: 10.5281/zenodo.3647587
- Zettergren, M. D., Semeter, J. L., & Dahlgren, H. (2015). Dynamics of density cavities generated by frictional heating: Formation, distortion, and instability. *Geophysical Research Letters*, 42(23).
- Zhang, Q.-H., Ma, Y.-Z., Jayachandran, P. T., Moen, J., Lockwood, M., Zhang, Y.L., . . . Xing, Z. Y. (2017). Polar cap hot patches: Enhanced density structures
  different from the classical patches in the ionosphere. *Geophysical Research*Letters, 44 (16), 8159-8167. doi: 10.1002/2017GL073439